INTRODUCTION: COMPUTATIONAL DOMAIN AND MEAN ATMOSPHERE

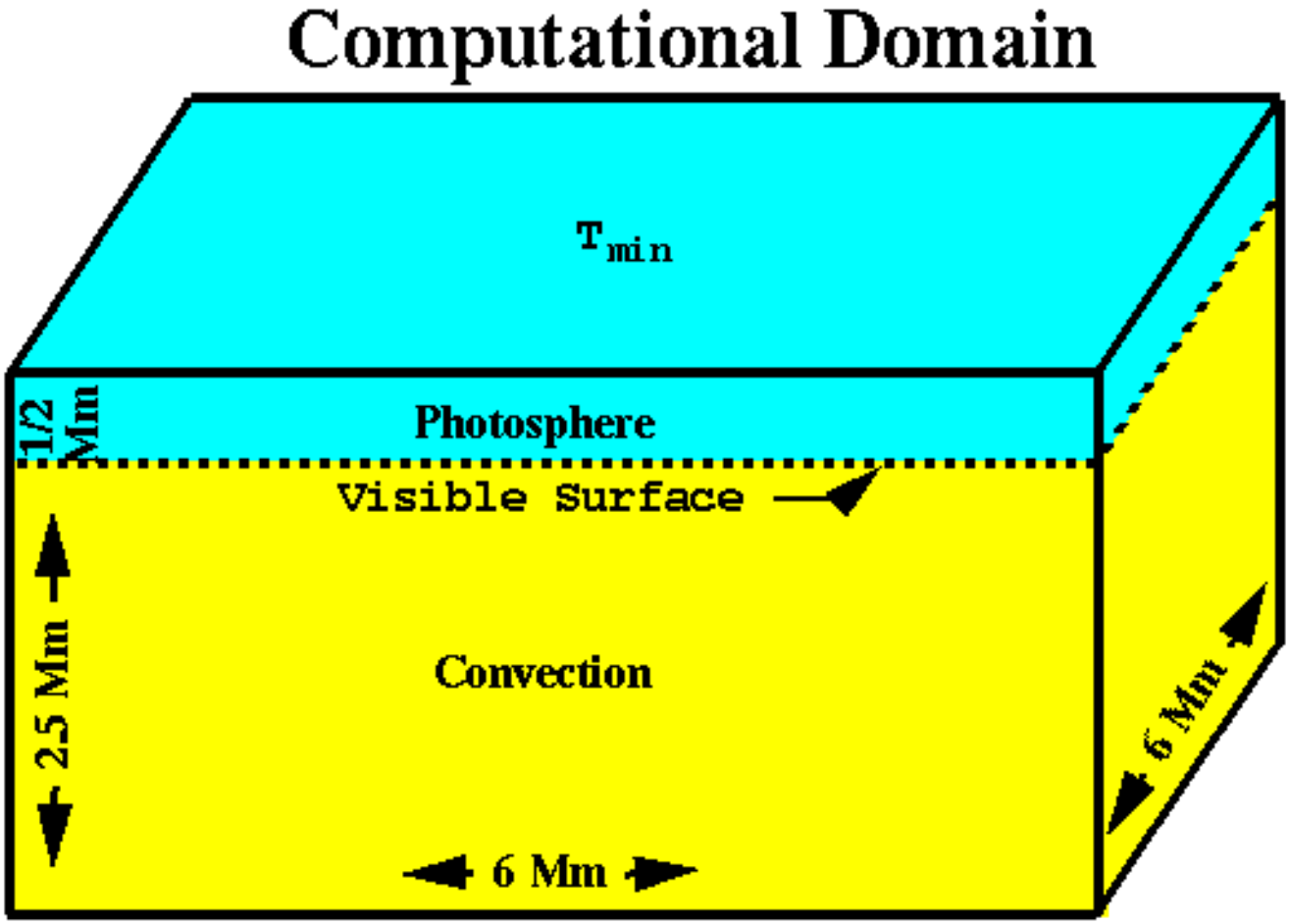

Figure 1: Simulation domain.

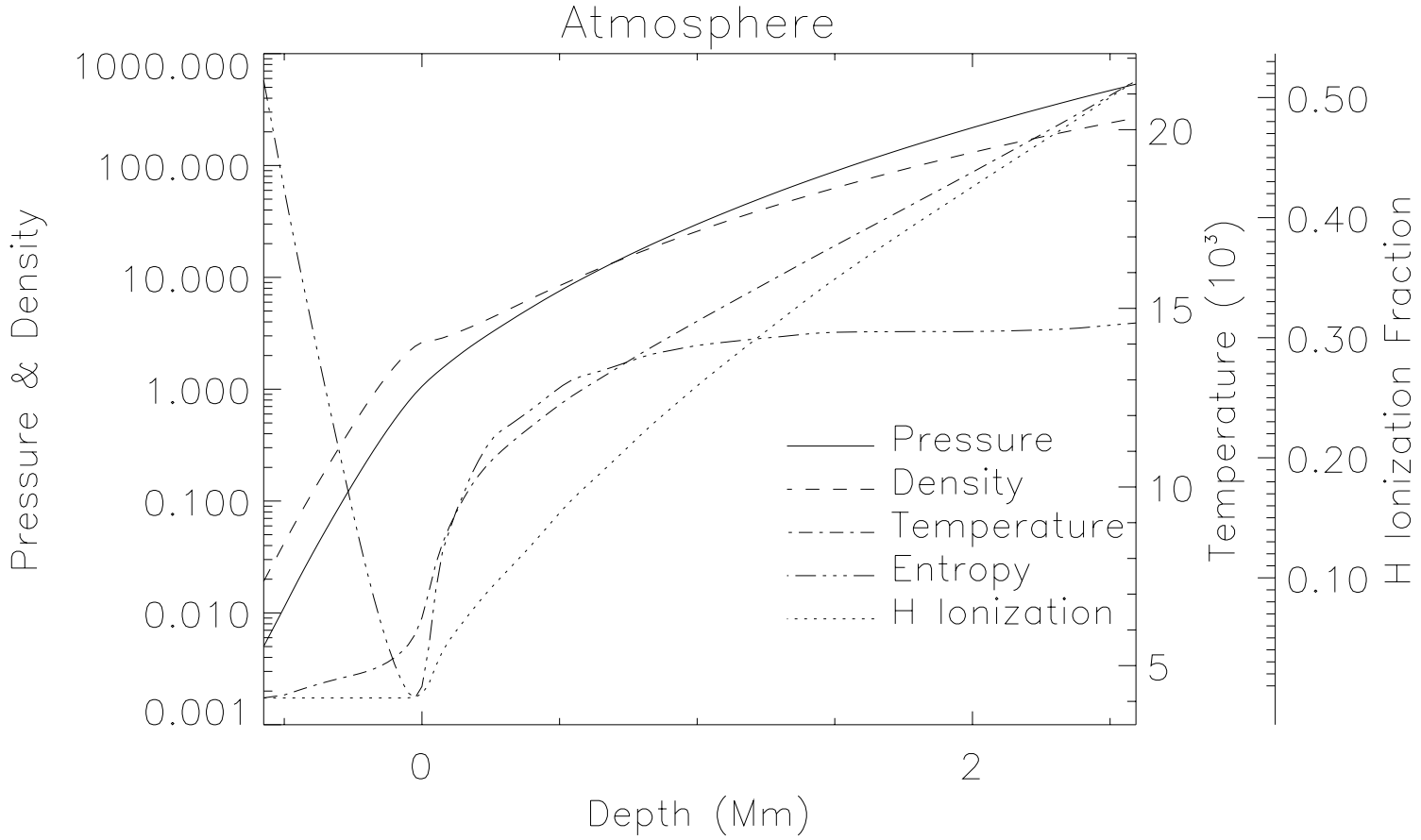

Figure 2: Mean atmosphere structure in the simulation. There are 10.8 pressure scale heights in the computational domain, 6 in the convective zone.

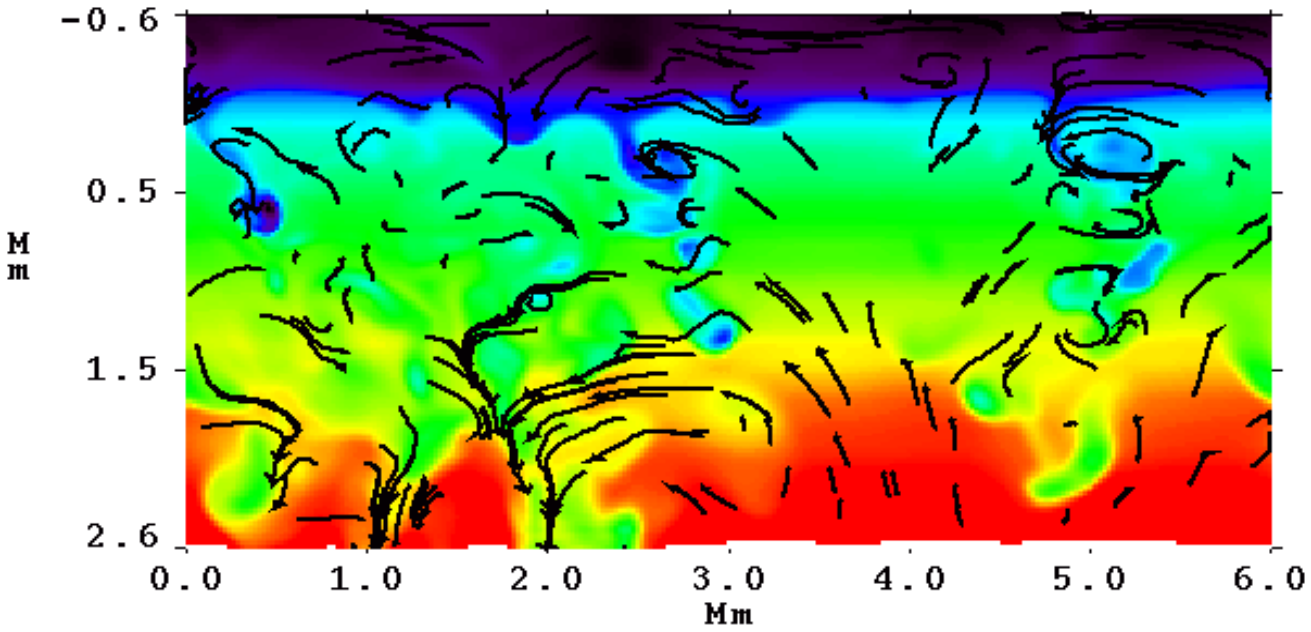

Figure 3: Topology of convection is warm, broad, fairly laminar, diverging upflows in which are embedded cool, narrow, turbulent, converging downflows. Upflows must turnover within about a scale height in order to conserve mass and they advect all passive properties into the downflow lanes.

ACTION IS IN THE INTERGRANULAR LANES

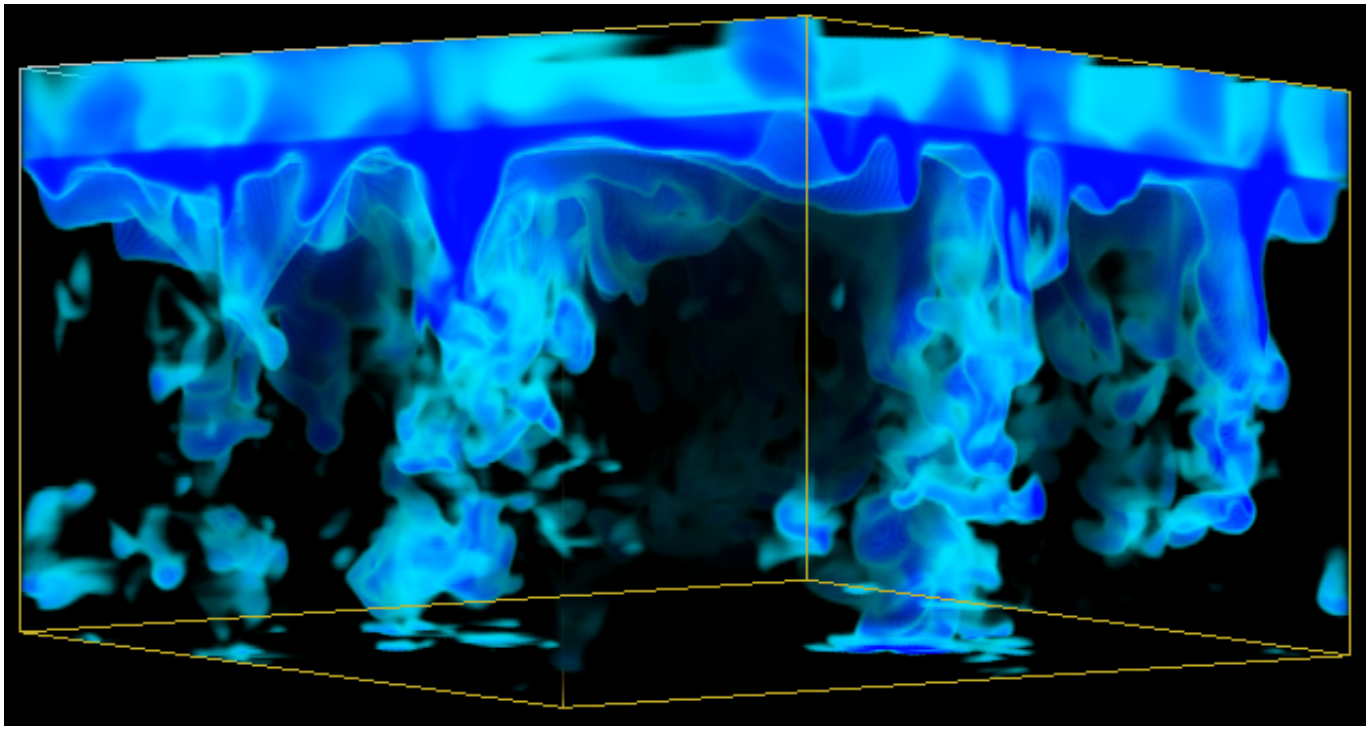

Figure 4: Entropy fluctuation image. Low entropy fluid is produced by radiative cooling in a thin surface thermal boundary layer. It forms the cores of dowdrafts and where most of the buoyancy work that drives the convection occurs.

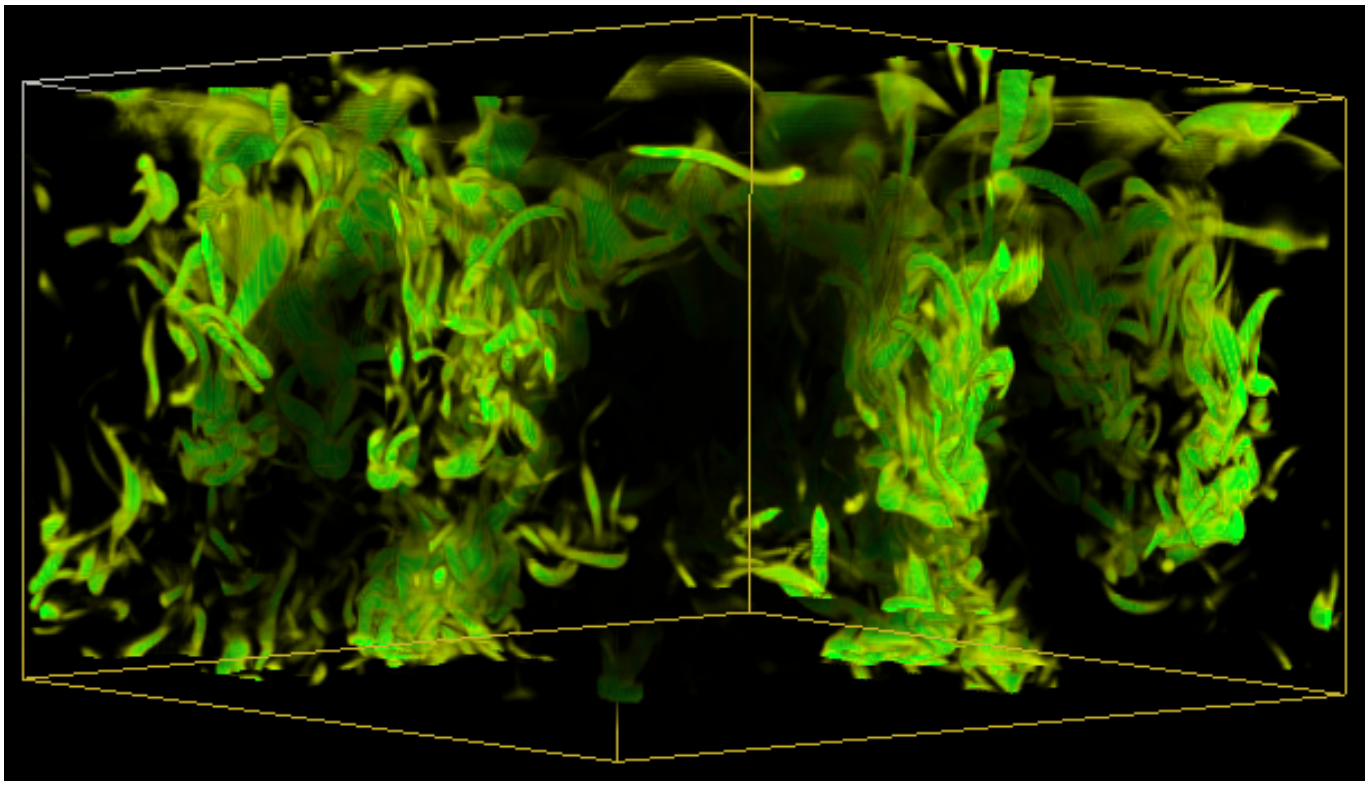

Figure 5: Vorticity image. Downdrafts are turbulent and uplows are fairly laminar.

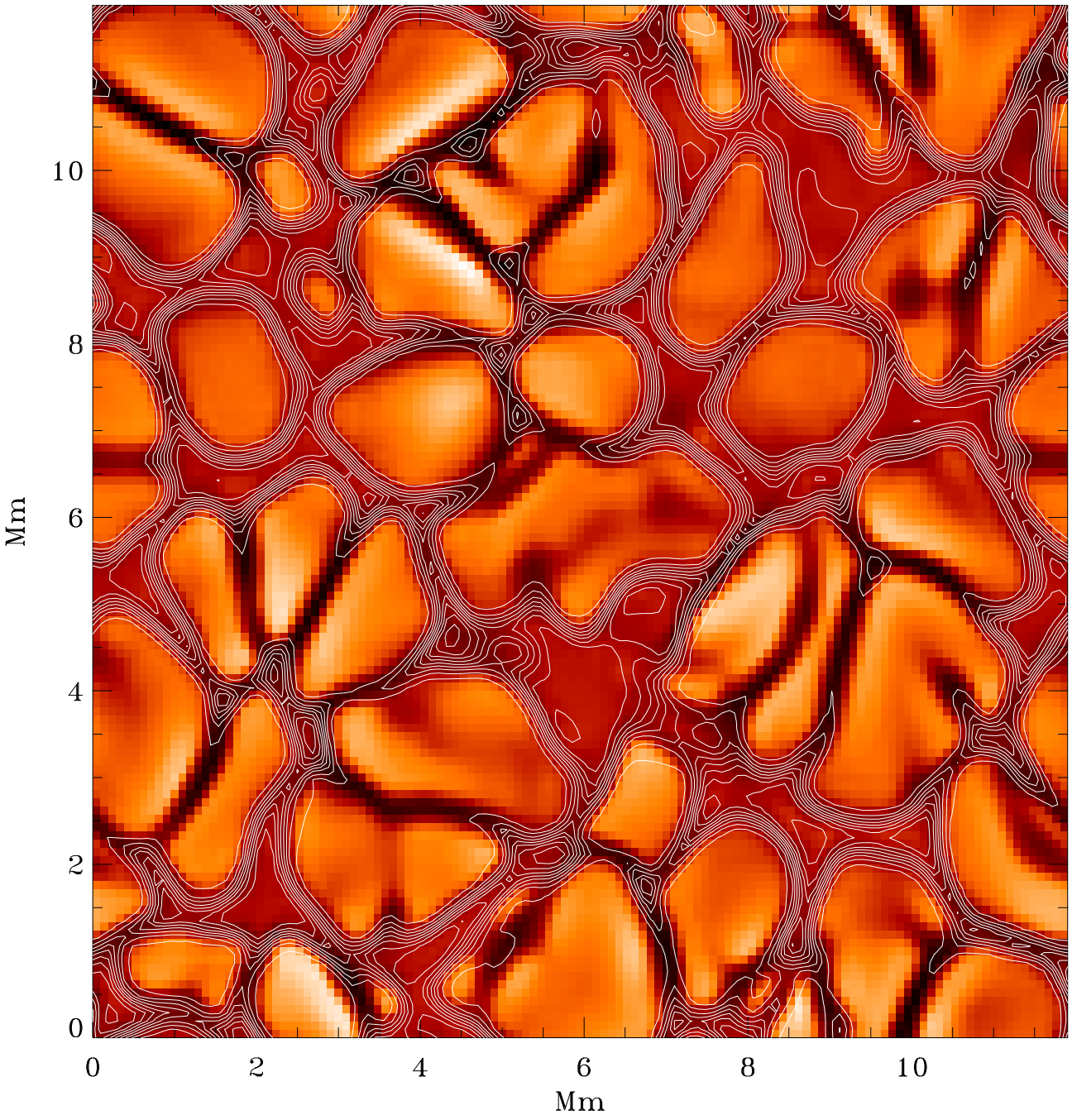

Figure 6: Image of surface vertical velocity with magnetic field contours, for initially uniform vertical field case. Magnetic field becomes confined to the intergranular downflow lanes, but does not entirely fill them.

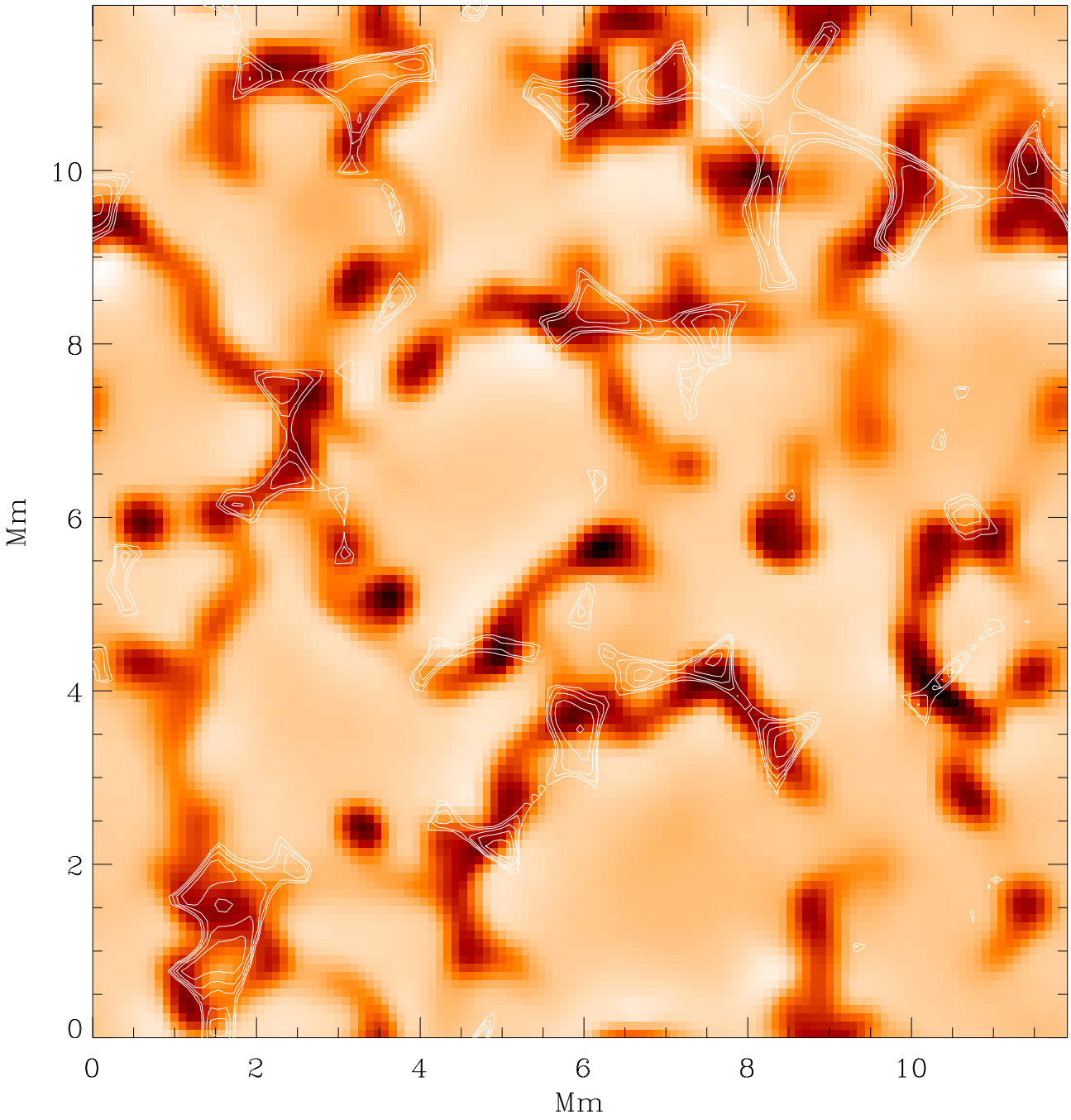

Figure 7: Image of vertical velocity 2.5 Mm below the surface with contours of magnetic field at the surface. The magnetic field is swept to the mesogranular boundary downflows.

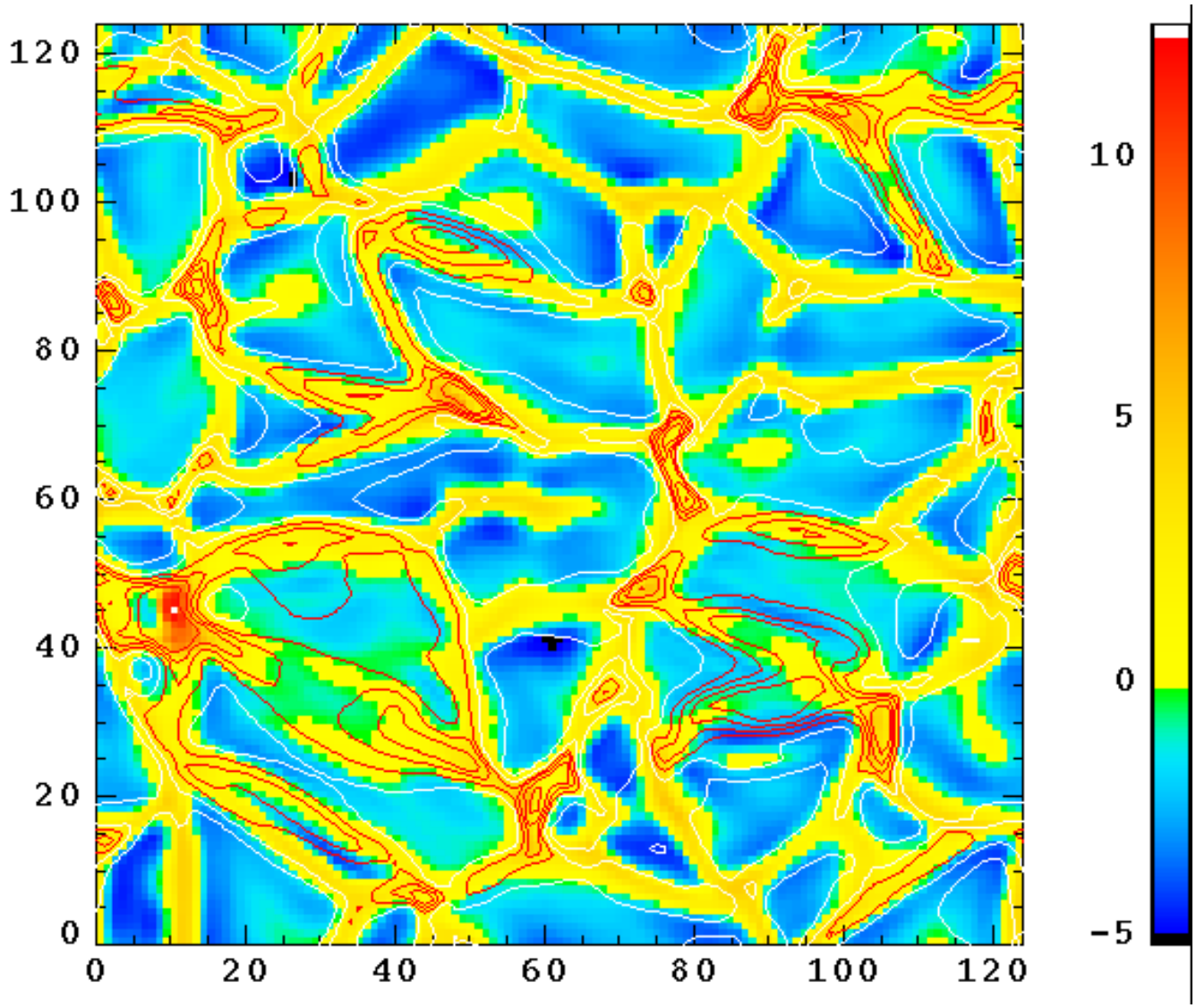

Figure 8: Surface vertical velocity and magnetic field contours, for advected horizontal field case. Again, the magnetic field is concentrated in the intergranular lanes.

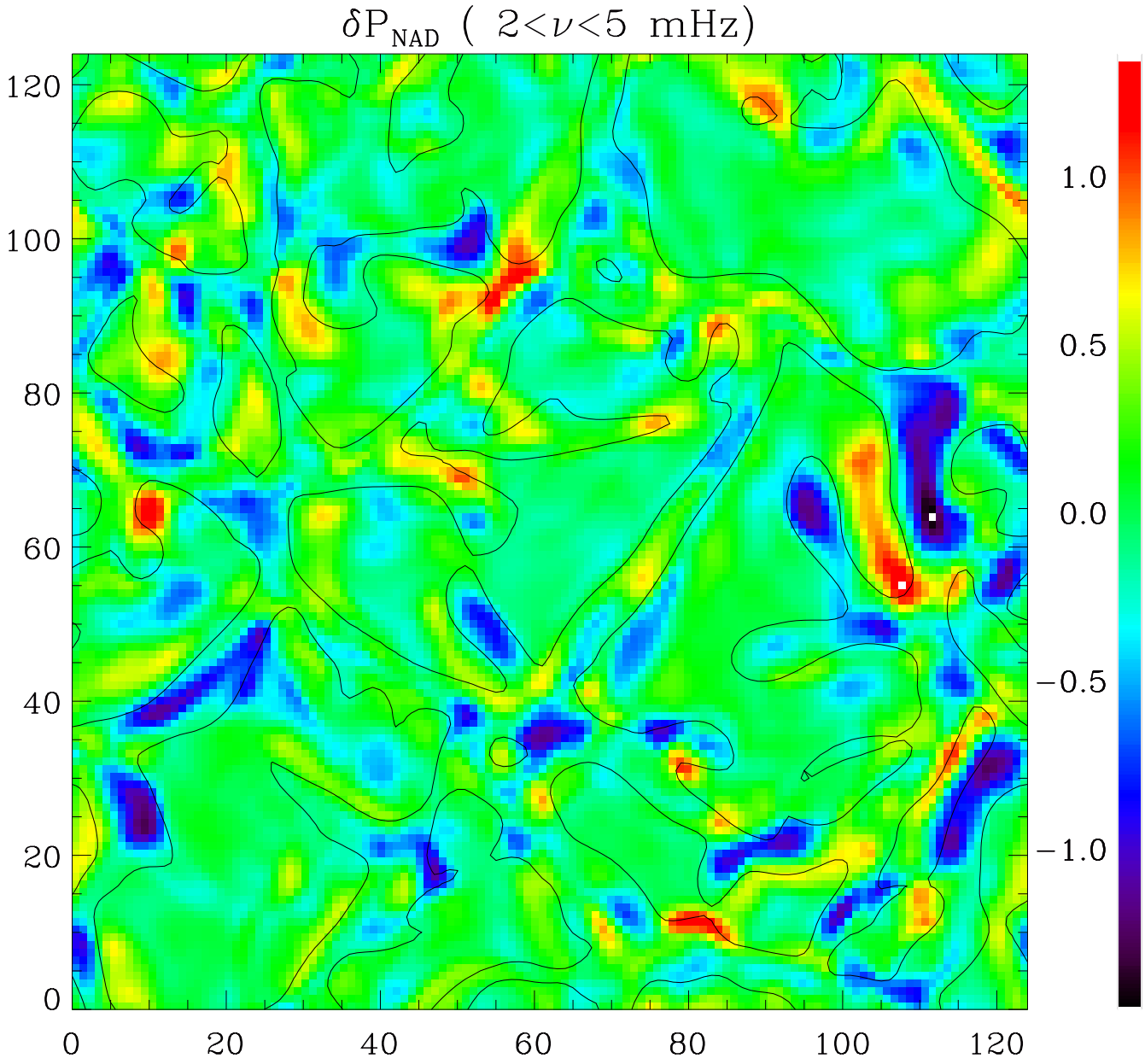

Figure 9: Sound generation occurs primarily in the intergranular lanes or at the boundaries of granules by the work of non-adiabatic pressure fluctuations. The dominant driver is turbulent pressure fluctuations.

$$\frac{d\langle E_\omega \rangle}{dt} = \frac{\omega^2 \left| \int_r dr \delta P_\omega^* \frac{\partial \xi_\omega}{\partial z} \right|^2}{8 \Delta\nu E_\omega} \ .$$

δP_ω = Fourier transform of the non-adiabatic pressure, E_ω = mode energy, ξ_ω = mode displacement eigenfunction, and $\Delta\nu$ = 1/(total time interval).

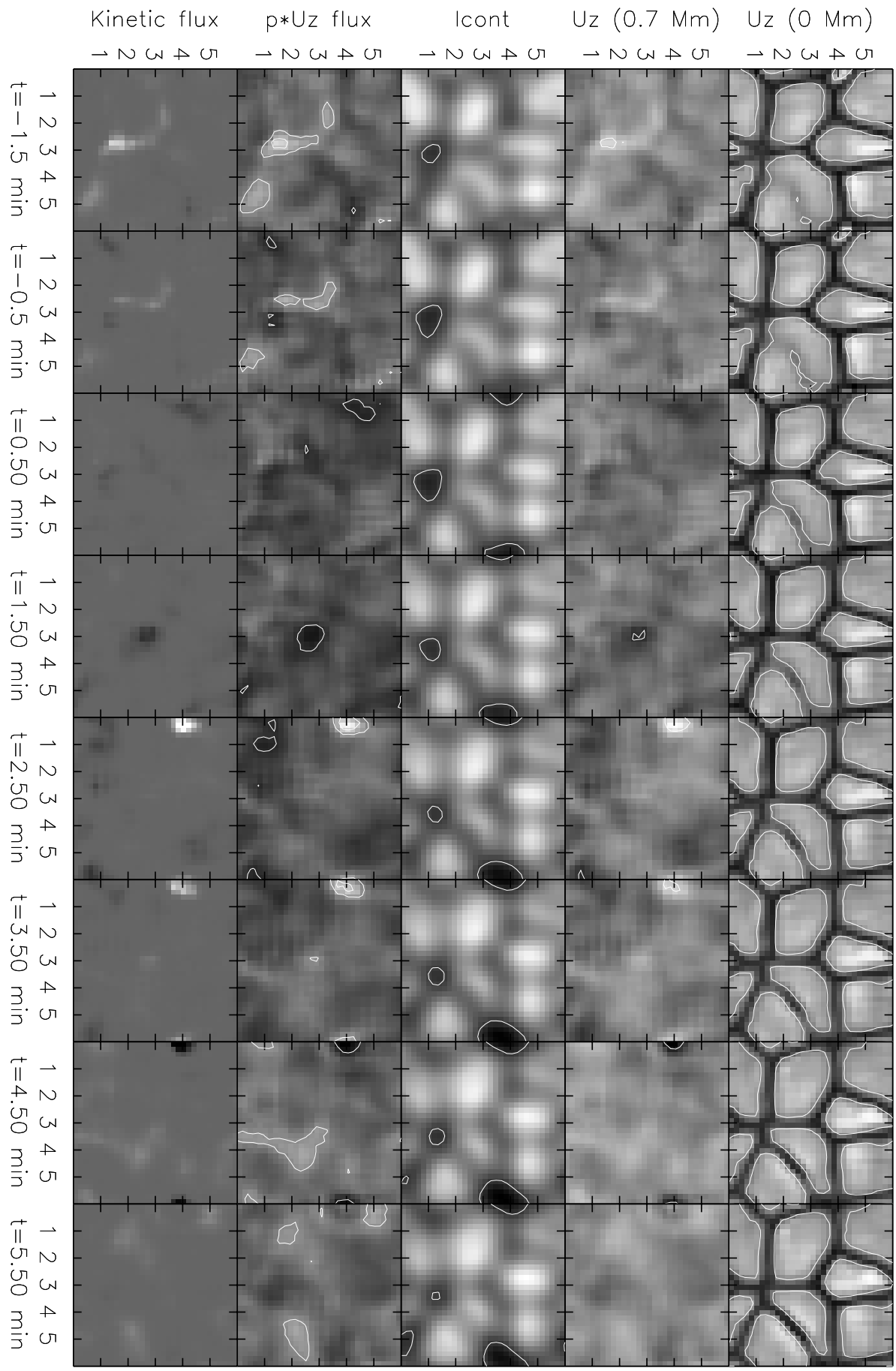

Figure 10: Acoustic events are generated by the collapse of small granules which produces a rarefaction followed by a compressive pulse that steepens into a shock in the chromosphere.

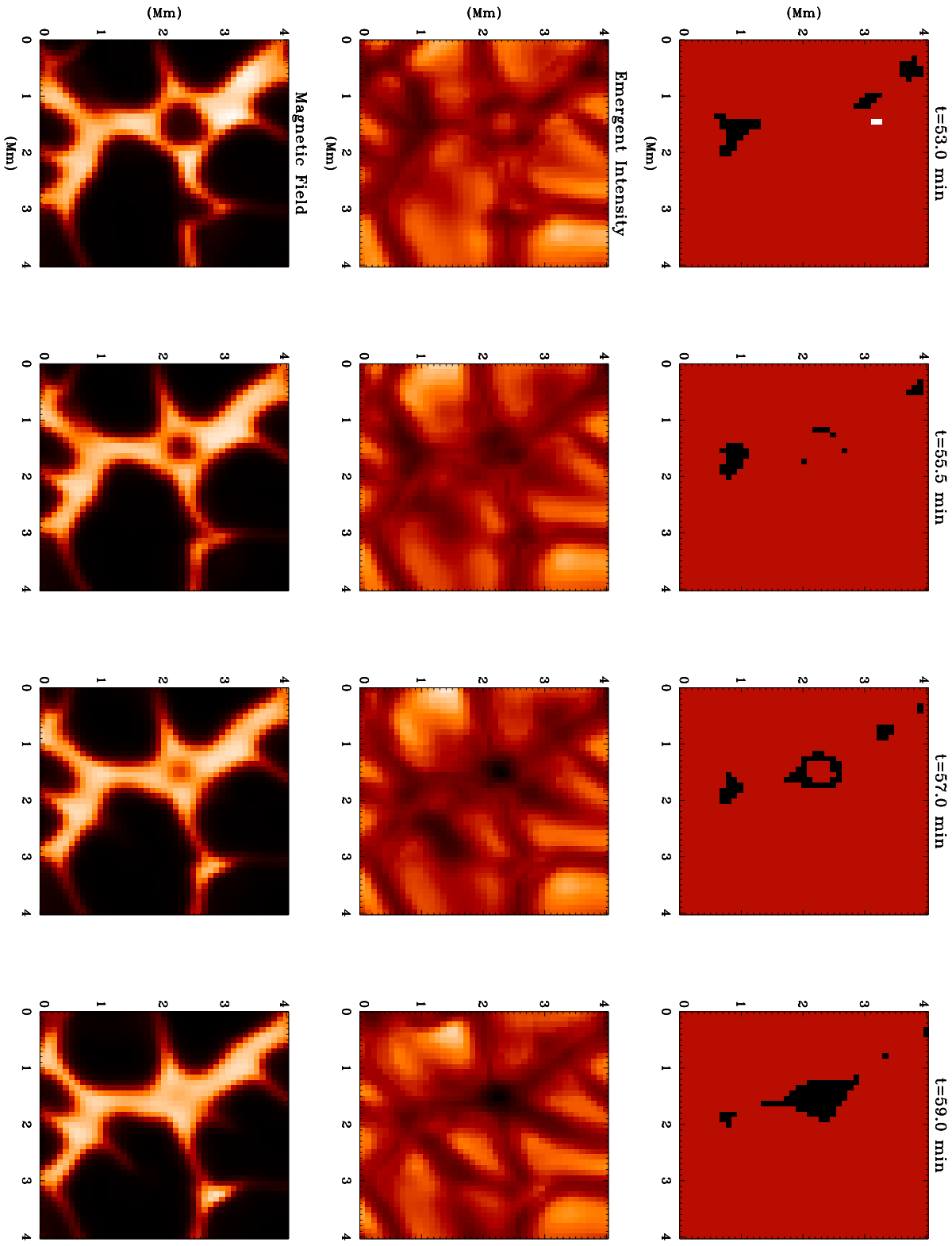

Figure 11: Micropores form in the intergranular lanes. Magnetic field (left), Intensity (center), darkest + strongest magnetic field (right). A tiny granule is squeezed out of existence as the magnetic field initially forms ring around it and then concentrates at the intergranular lane vertex when the granule disappears.

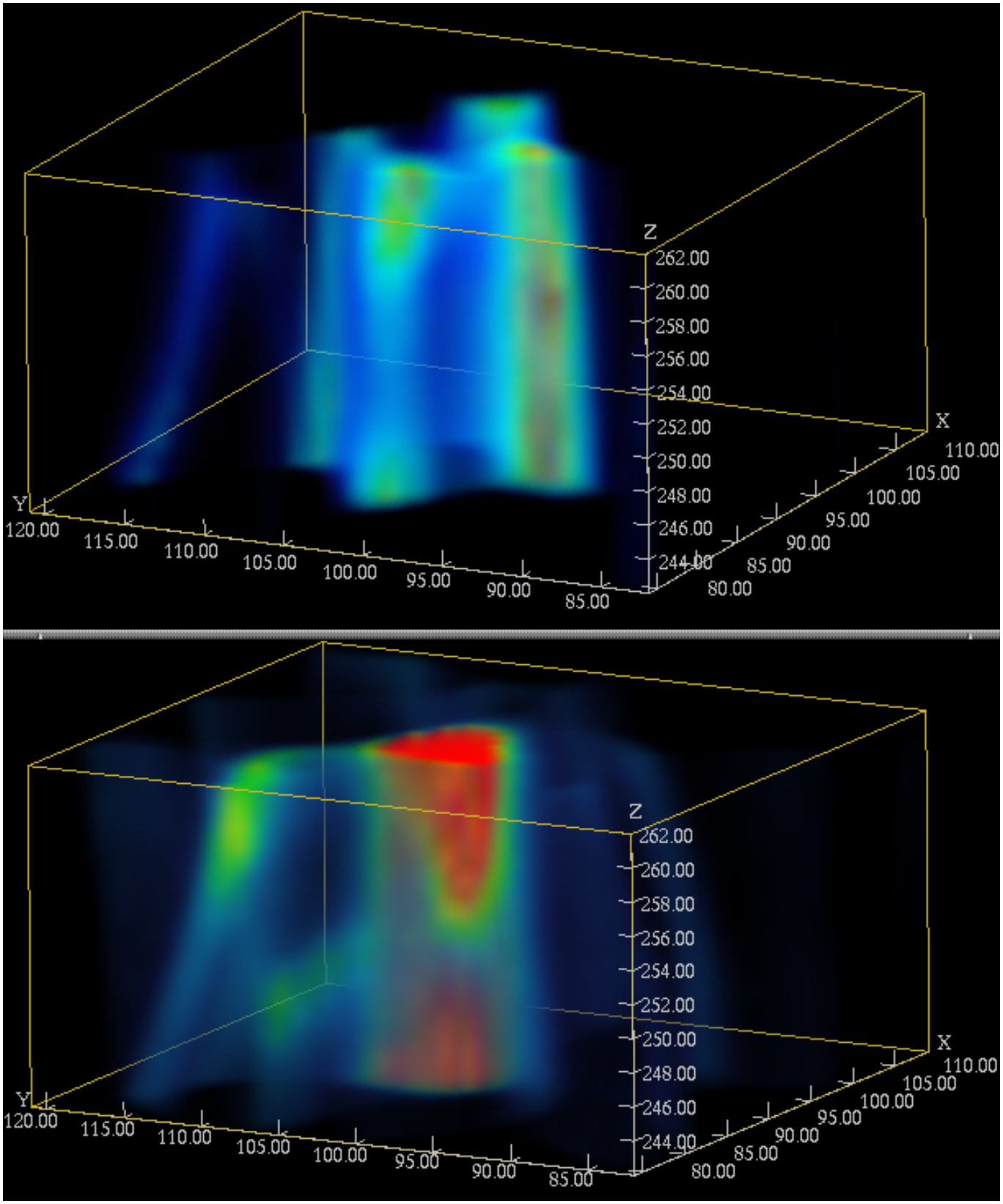

Figure 12: Pore forming in between four magnetic flux concentrations. Surface magnetic field (top), intensity (bottom, red = darkest) as a function of time (increasing upwards).

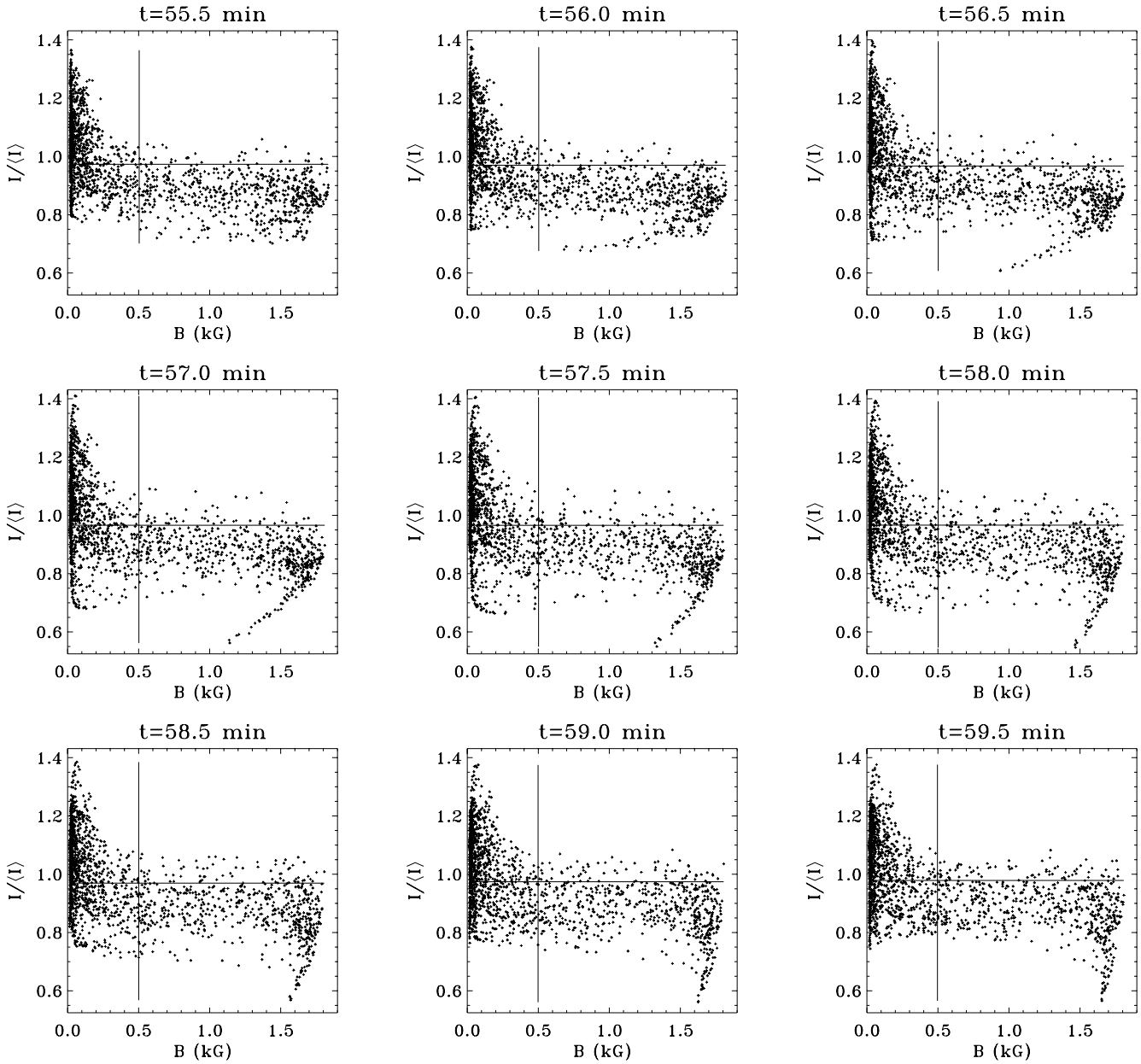

Figure 13: Intensity vs. magnetic field strength during pore formation. The dark pore forms first where the field is weak and the field strength gradually increases over time.

ACTION IS CLOSE TO THE SURFACE

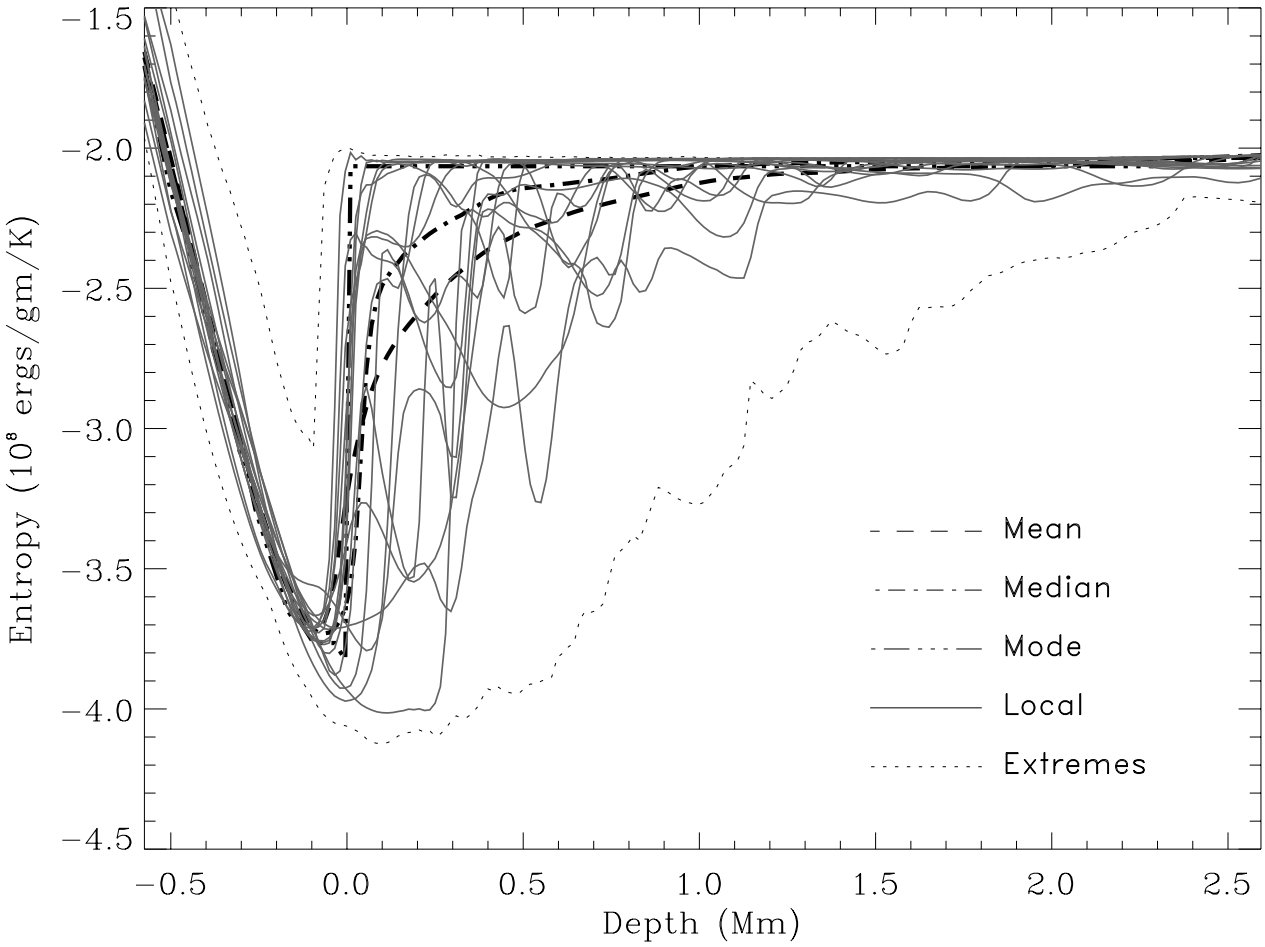

Figure 14: Low entropy fluid is produced by radiative cooling in a thin surface thermal boundary layer and forms the cores of the downdrafts. Entropy fluctuations decrease with depth due to energy diffusion and mixing with entropy neutral ascending fluid that turns over and becomes entrained in the downdrafts.

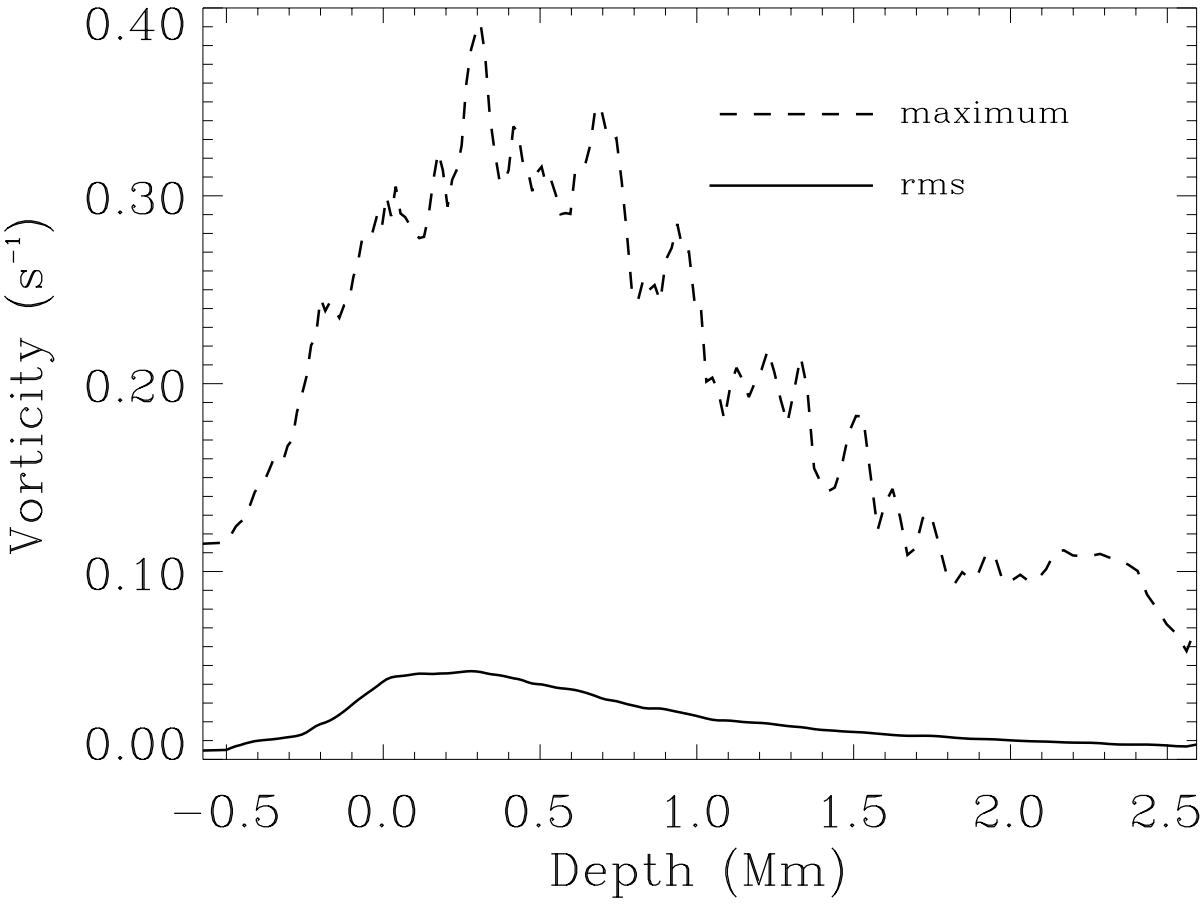

Figure 15: Vorticity as a function of depth. Vorticity decreases with increasing depth because the velocities decrease as the density increases.

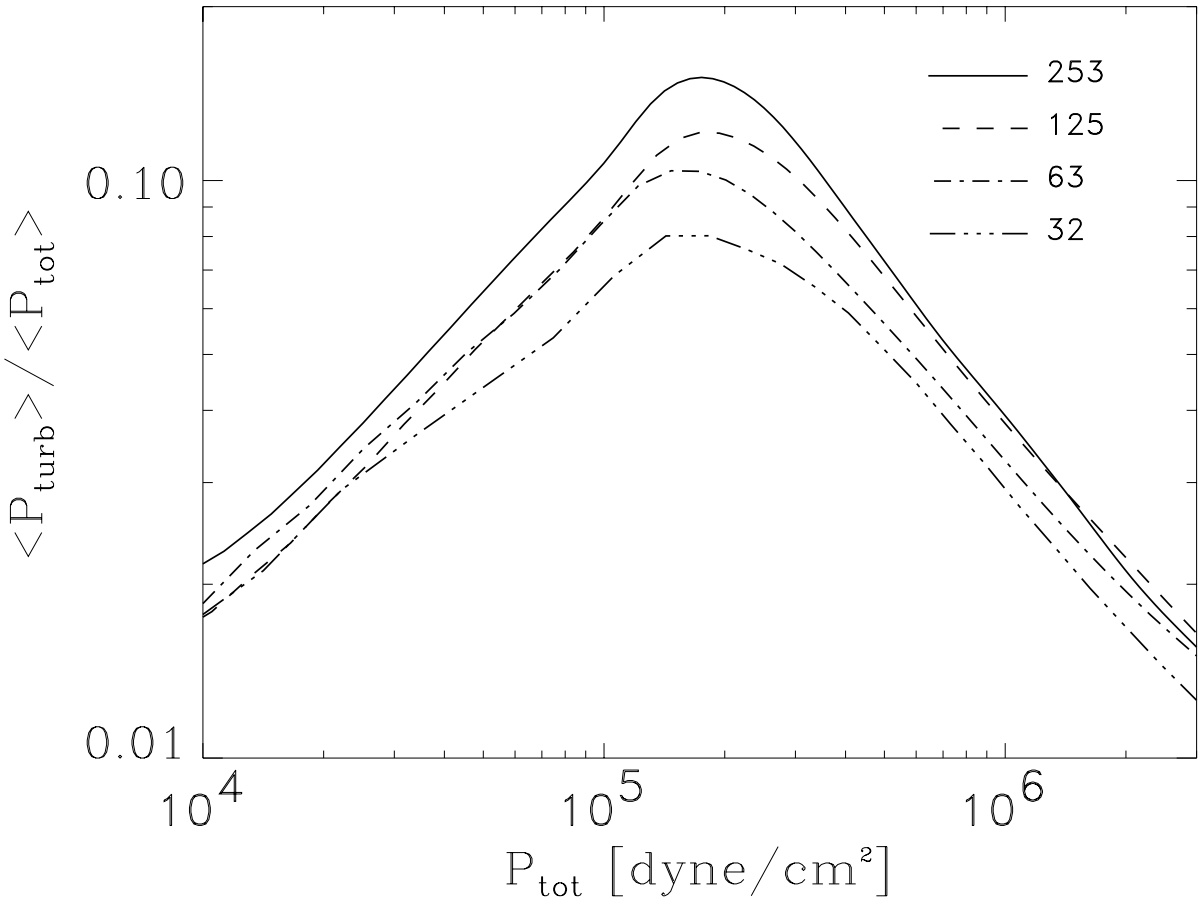

Figure 16: Turbulent pressure peaks close to the surface and then decreases relative to the total pressure.

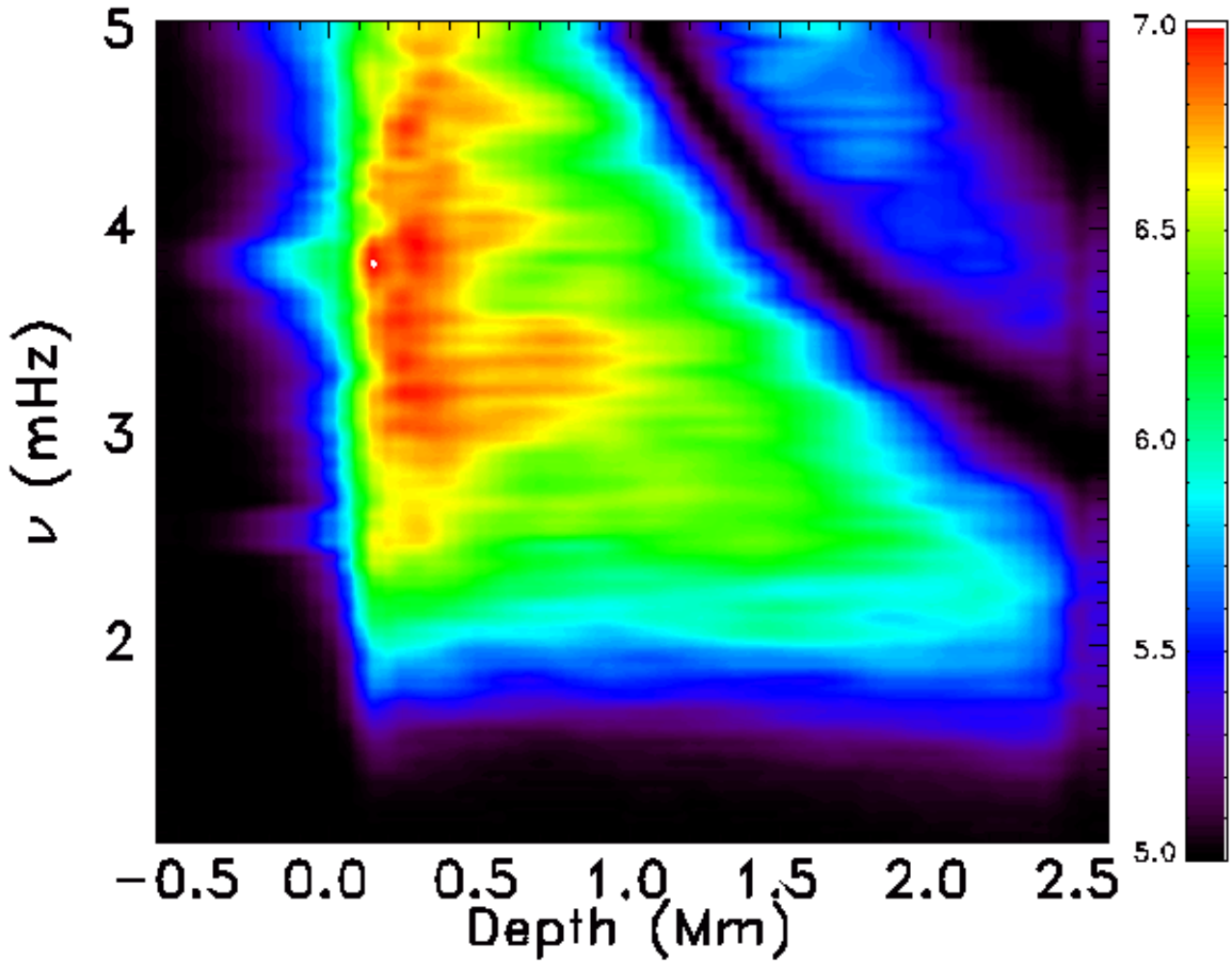

Figure 17: Sound generation is concentrated close to the surface in the peak excitation range (3 - 4 mHz) and at higher frequencies. Logarithm (base 10) of the work integrand, $\omega^2 \left|\delta P_\omega^* \frac{\partial \xi_\omega}{\partial z}\right|^2 / 8\Delta\nu E_\omega$, as a function of depth and frequency, (in units of ergs/cm^2/s).

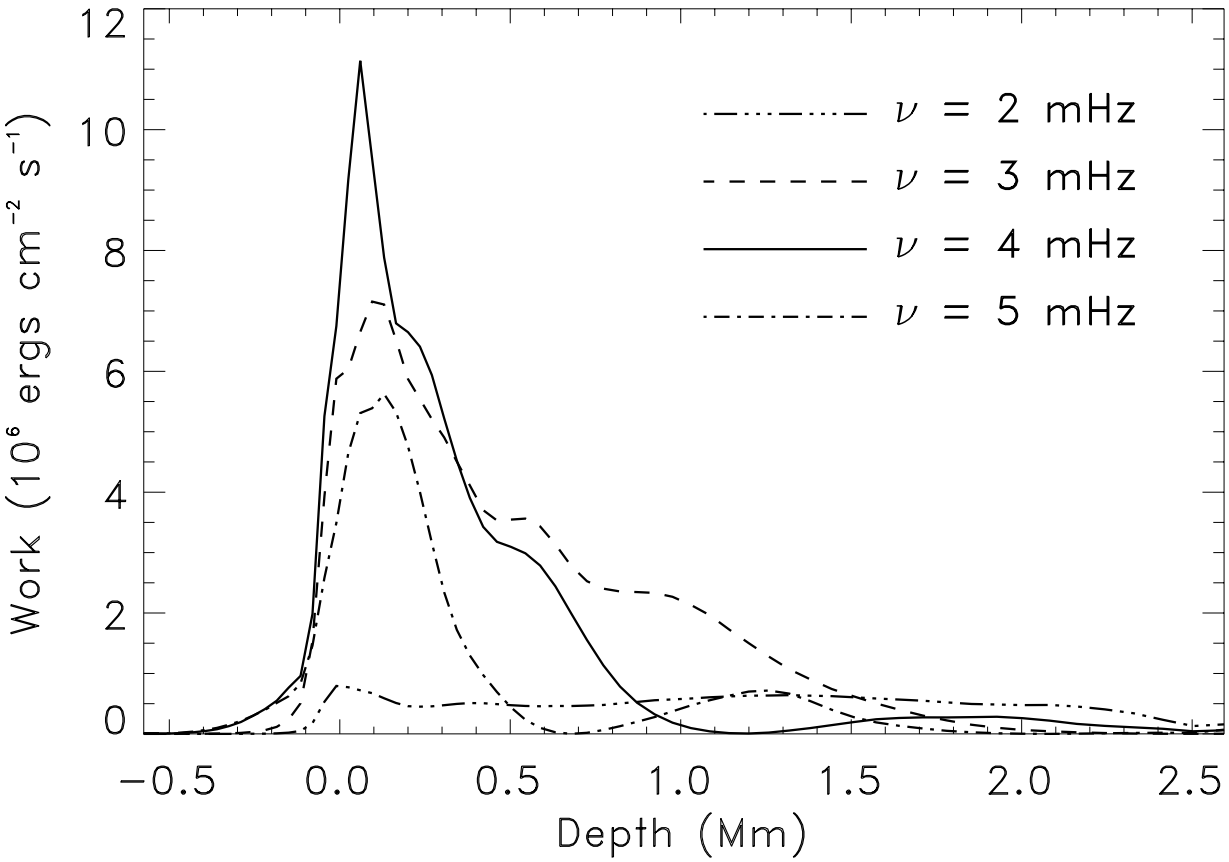

Figure 18: Integrand of the work integral at 2, 3, 4, and 5 mHz as a function of depth. At frequencies where the driving is large, the integrand is significant only within 500 km of the surface.

COMPARISON WITH OBSERVATIONS

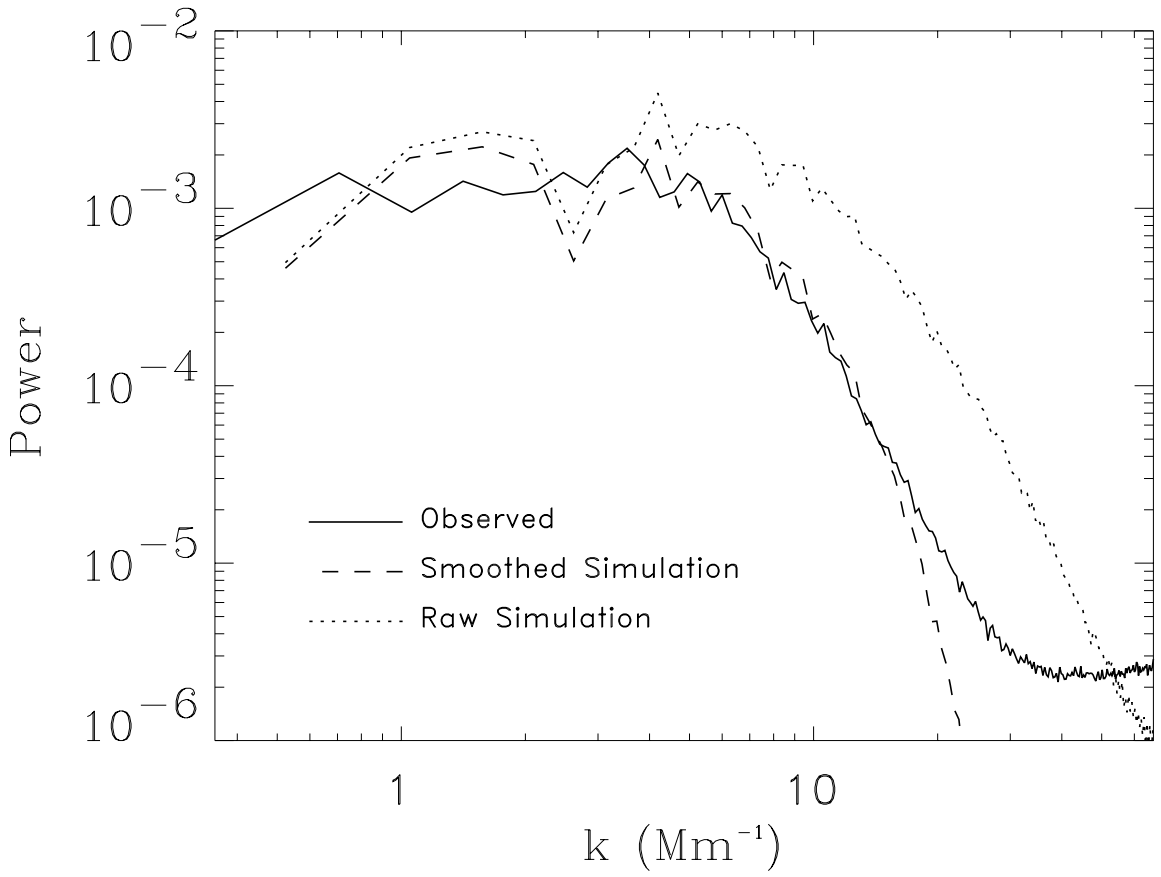

Figure 19: Size spectrum of observed and simulated granules including effects of smoothing by the point spread function.

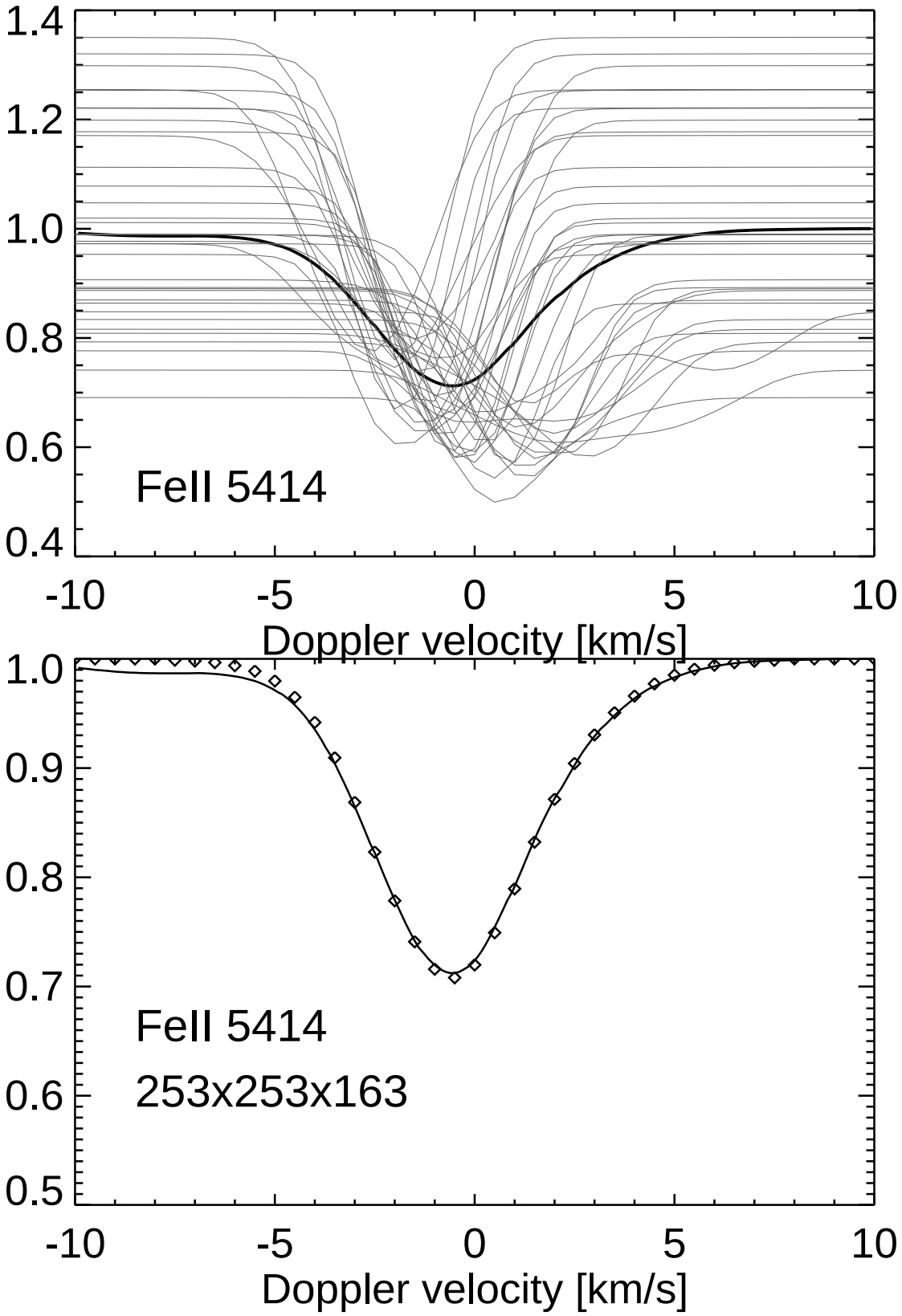

Figure 20: Overshooting convective motions produce line broadening and shifting and lead to the observed mean FeII 541.4 nm line, without any micro- or macro- turbulence or additional damping.

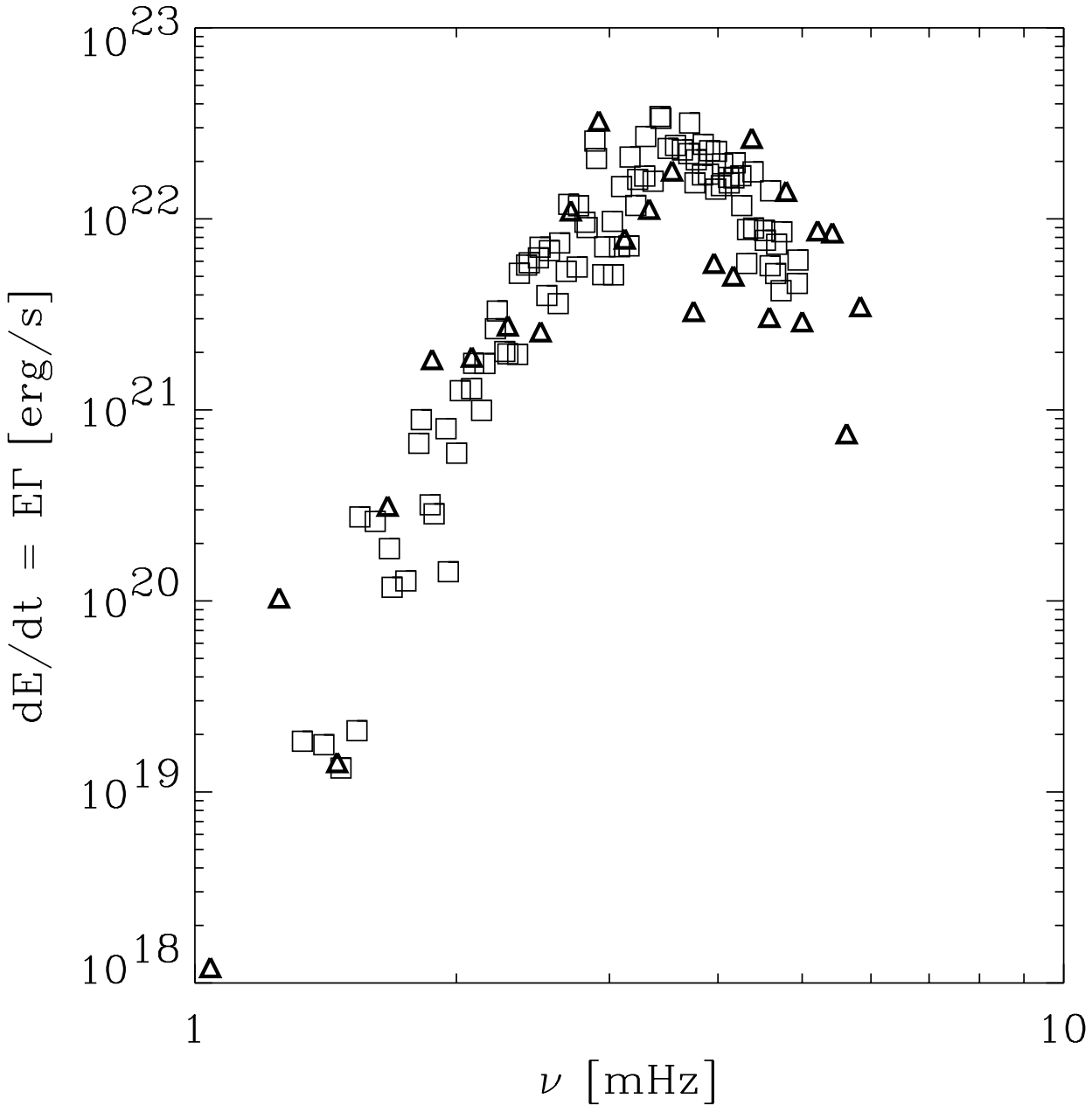

Figure 21: Rate of stochastic energy input to radial p-modes for the entire solar surface, Simulation=triangles, observations=squares (from Roca Cortes (1999), based on observed mode velocity amplitudes and line widths from GOLF, for modes $\ell = 0 - 3$, which are nearly radial close to the surface).

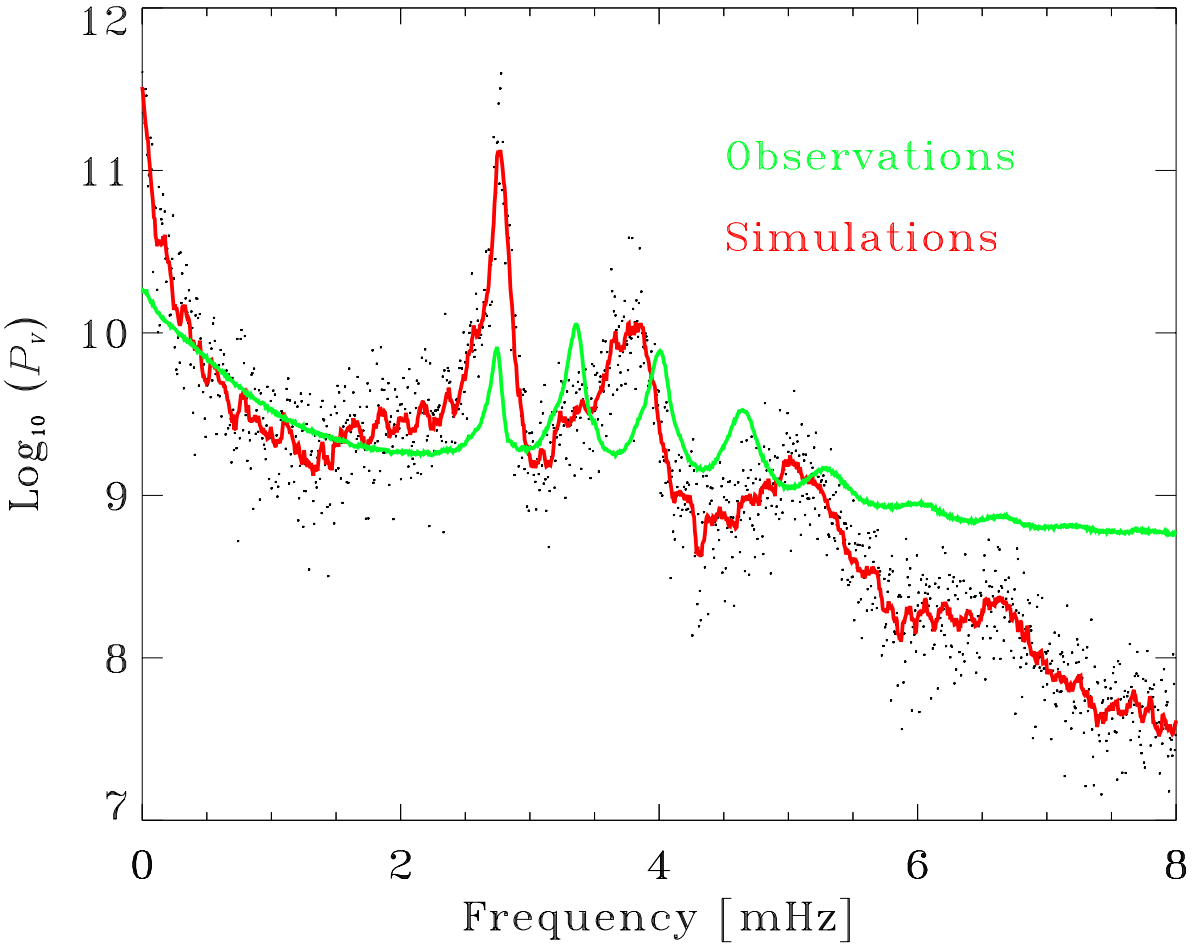

Figure 22: Velocity power spectrum for $\ell = 740$ modes. Units are (cm s^{-1})^2 Hz^{-1}. Observed velocities are from MDI, summed over all $2\ell + 1$ m-modes. Simulation was run for 43 hours of solar time. The modes are asymmetric, as is observed, with more power on the low frequency side. The simulated modes are sparser and broader than the observed modes because the simulation domain is shallow.

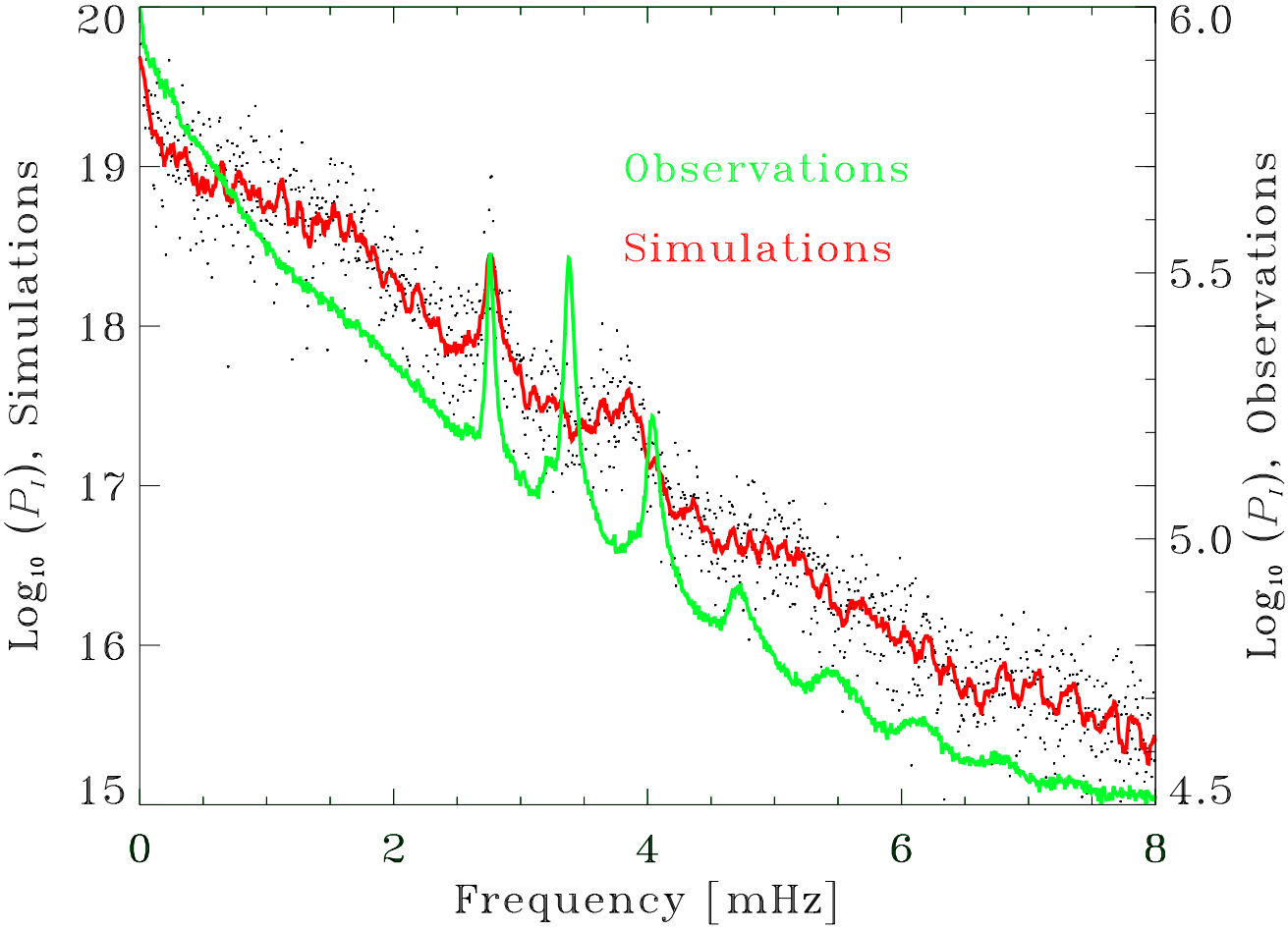

Figure 23: Intensity power spectrum for $\ell = 740$ modes. Intensity has the opposite asymmetry to the velocity, with more power on the high frequency side.

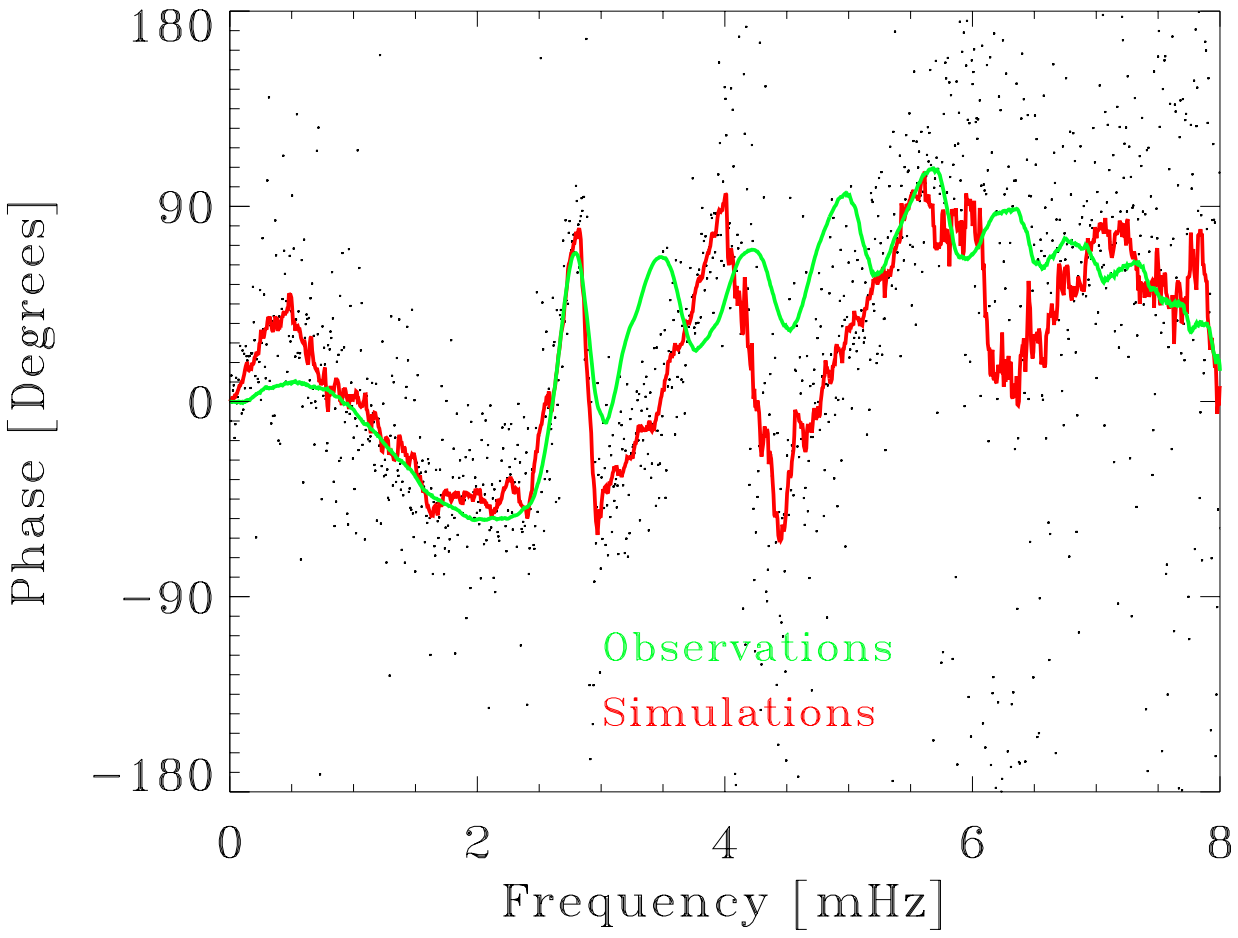

Figure 24: Velocity - Intensity phase for $\ell = 740$ modes.

MAGNETO-CONVECTION

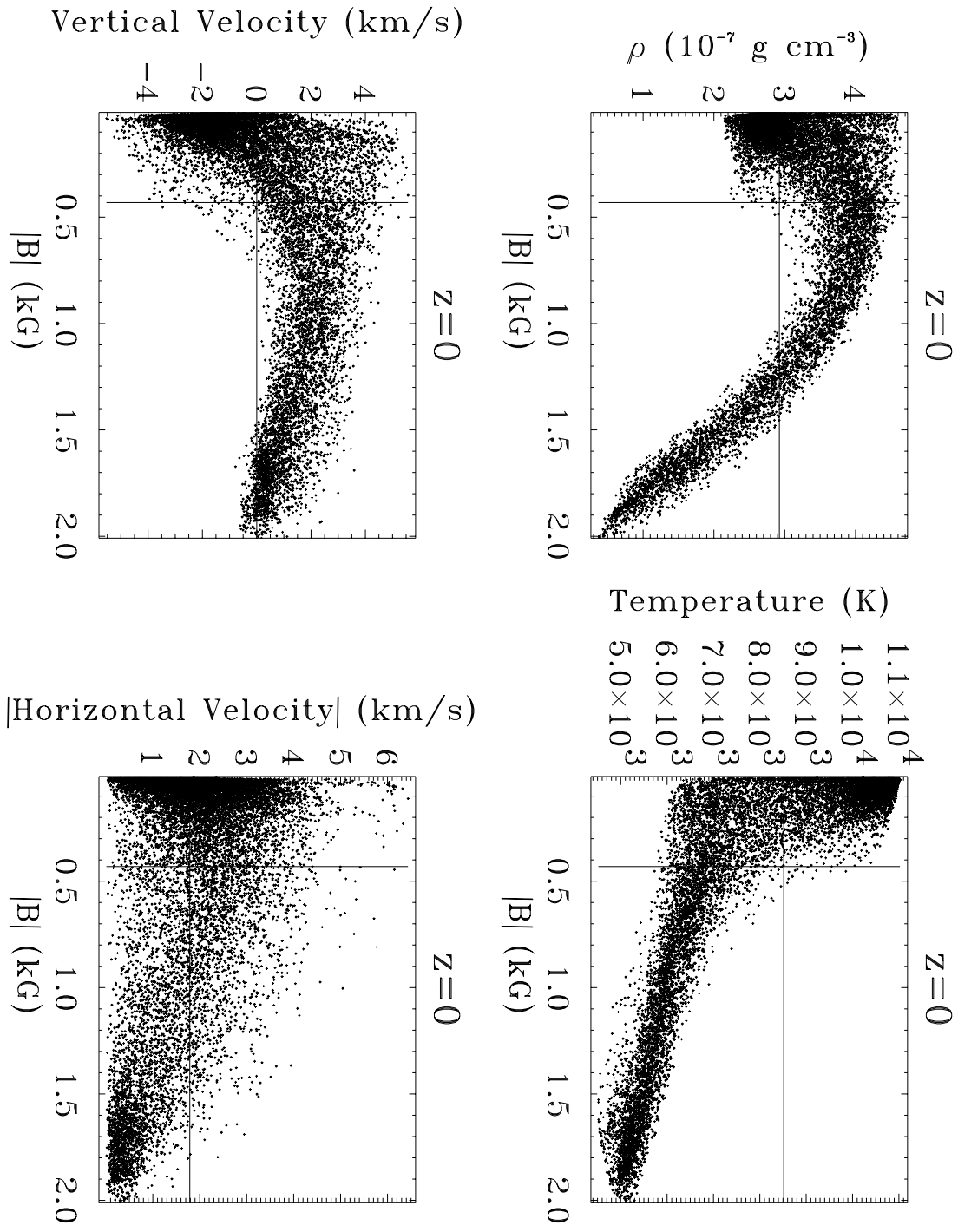

Figure 25: At a fixed geometric height ($< \tau >= 1$), where the field is strong the density is smaller, the temperature is lower, and the flow is suppressed and is downwards ($V_z > 0$).

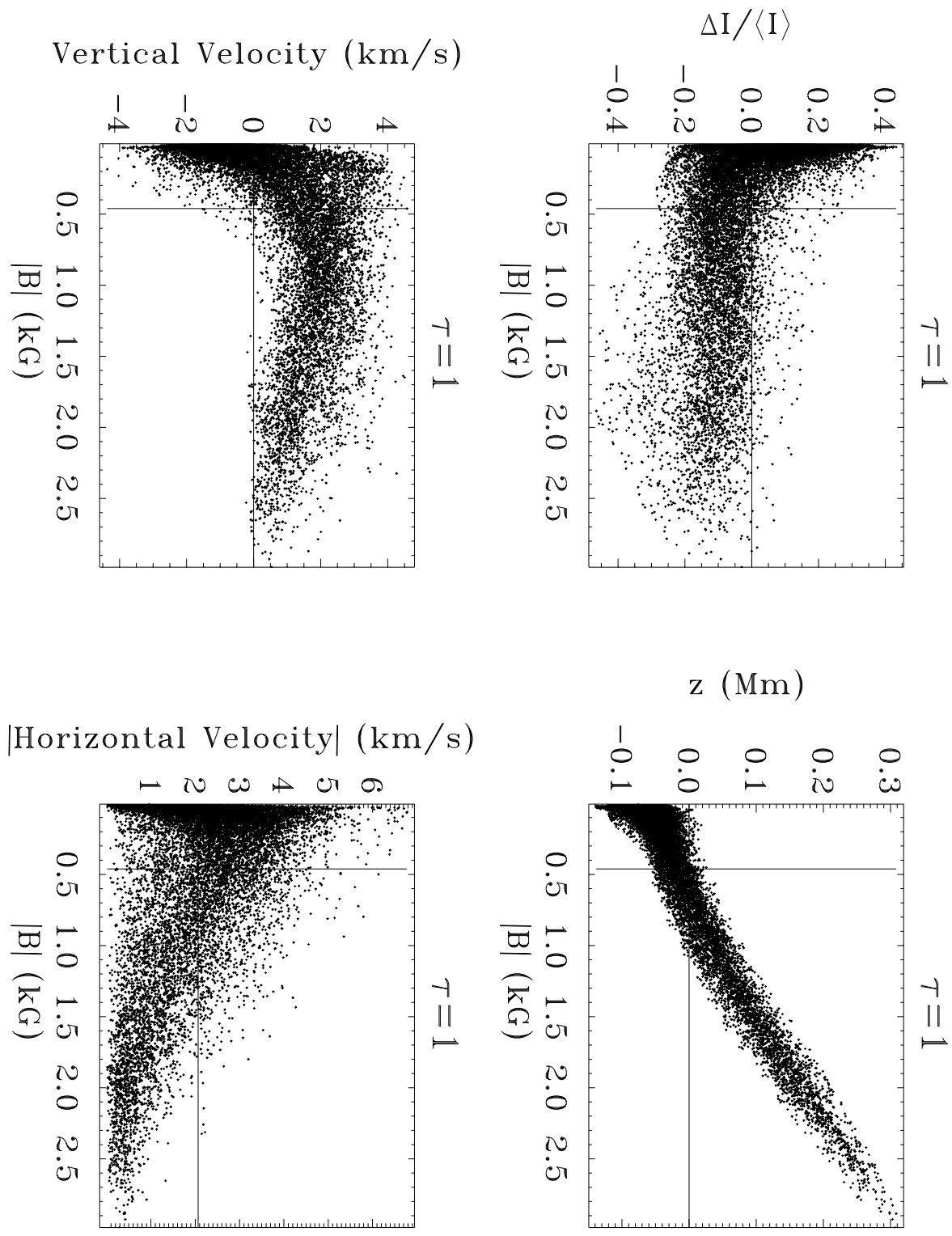

Figure 26: Strong magnetic field locations are darker, suppress both the vertical and horizontal velocity and the $\tau = 1$ surface lies deeper by several hundred kilometers.

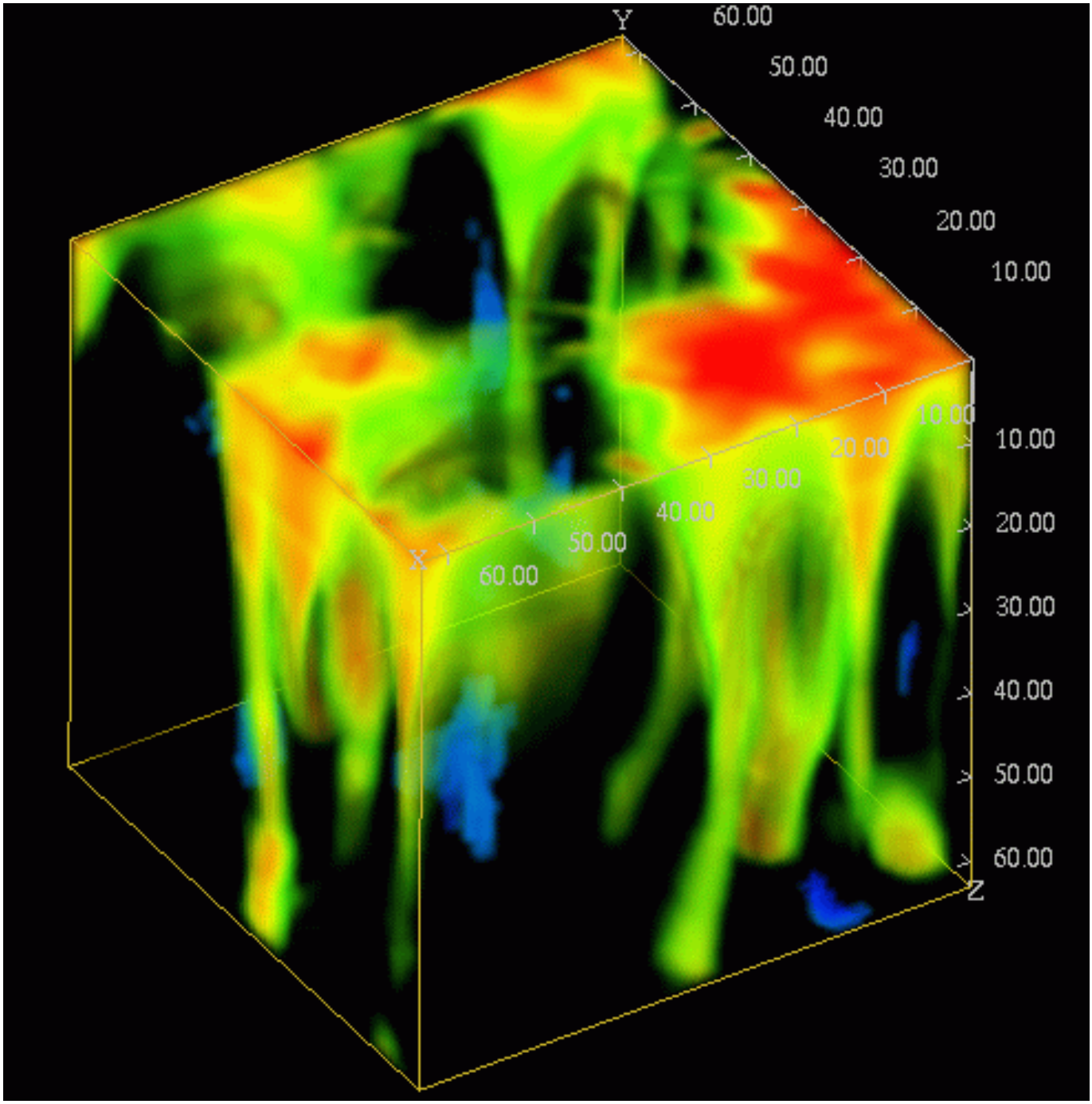

Figure 27: 3D image of magnetic field. Magnetic flux tubes have a filamentary structure.

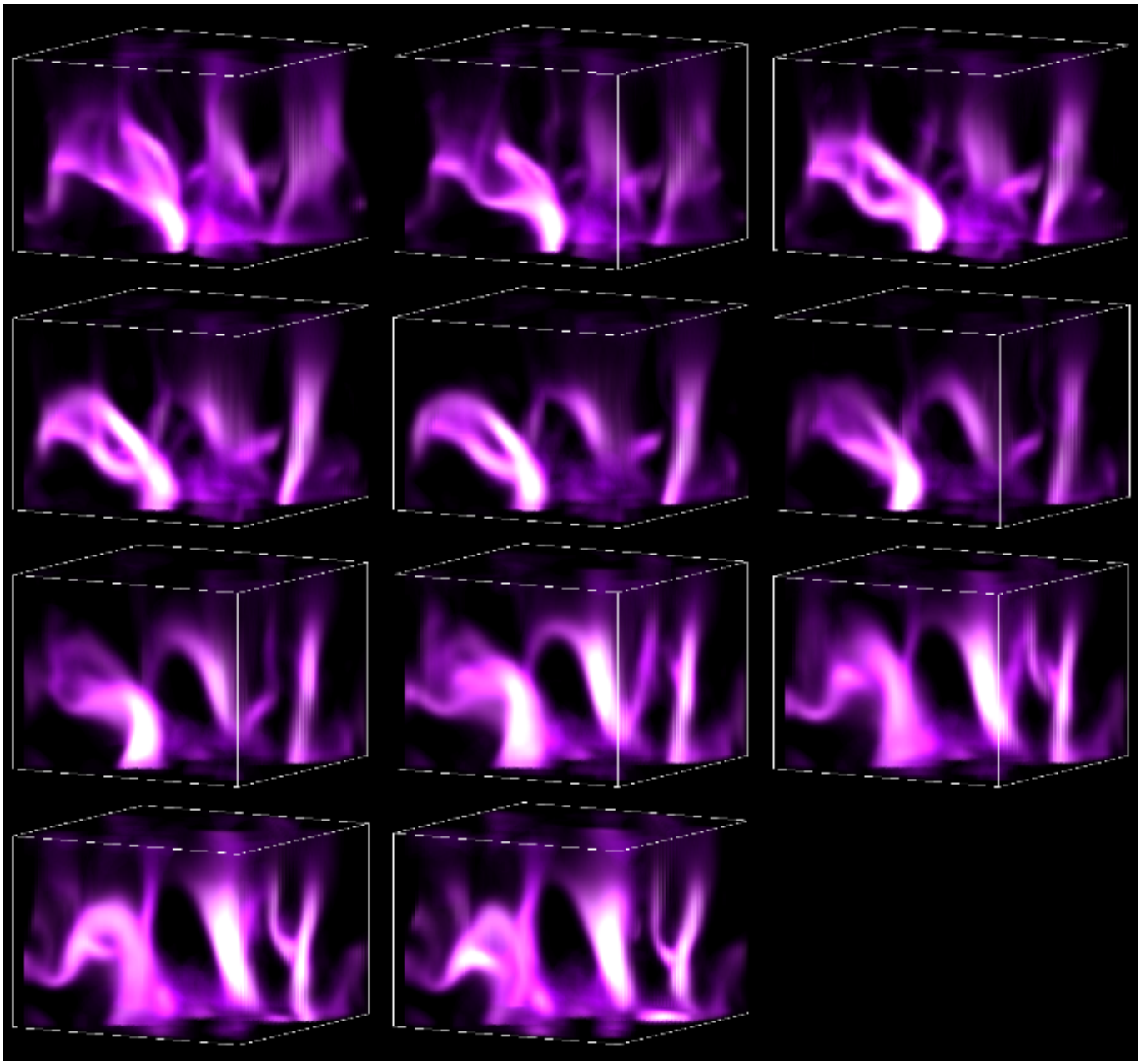

Figure 28: Magnetic field loops rising through the solar surface and opening.

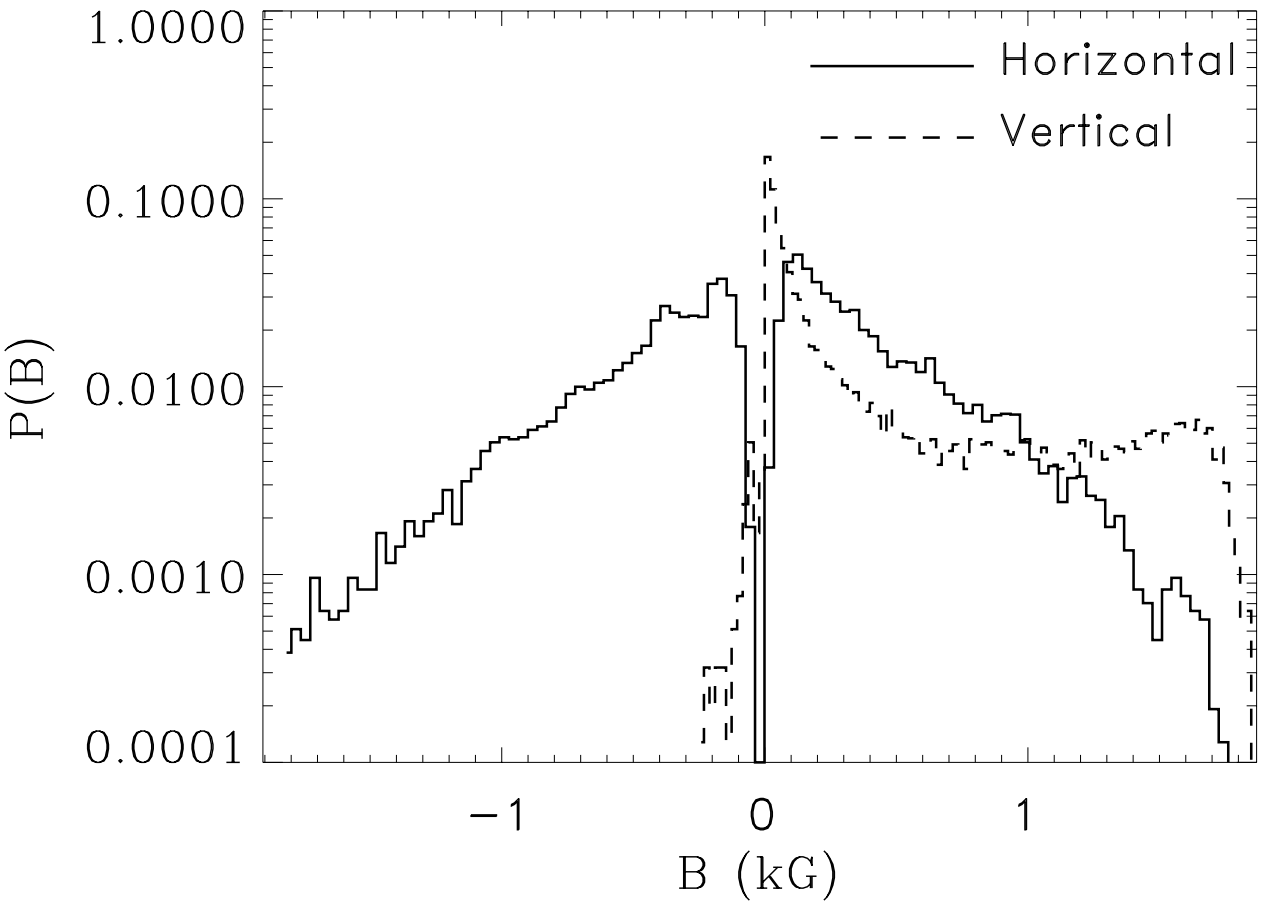

Figure 29: Probability distribution of surface magnetic field for both case of imposed mean vertical field and inflow horizontal field. The inflow horizontal field case shows an exponential distribution. The imposed mean vertical field case has a very narrow exponential distribution from dynamo activity and a broad secondary peak at strong fields due to the concentration of the imposed mean field.

MICROPORES

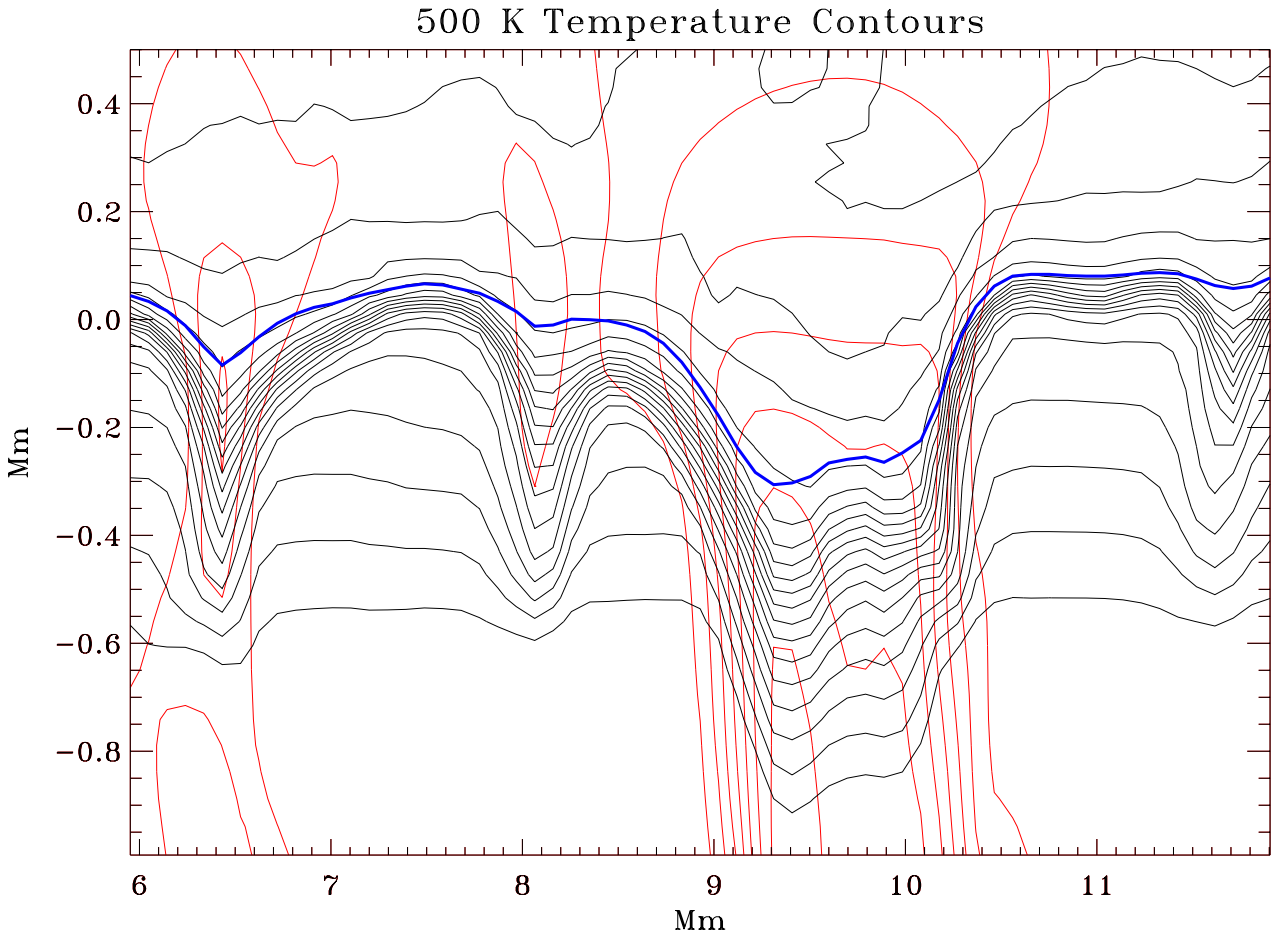

Figure 30: Temperature and magnetic field contours (red) in bright point (left) and micropore (right). Temperature is lower in the bright point and micropore. Blue line is optical depth unity, which is depressed in the both the bright point and micropore. The $\tau = 1$ level cuts the bright point at a higher temperature than the surroundings and cuts the micropore at a lower temperature than the surroundings.

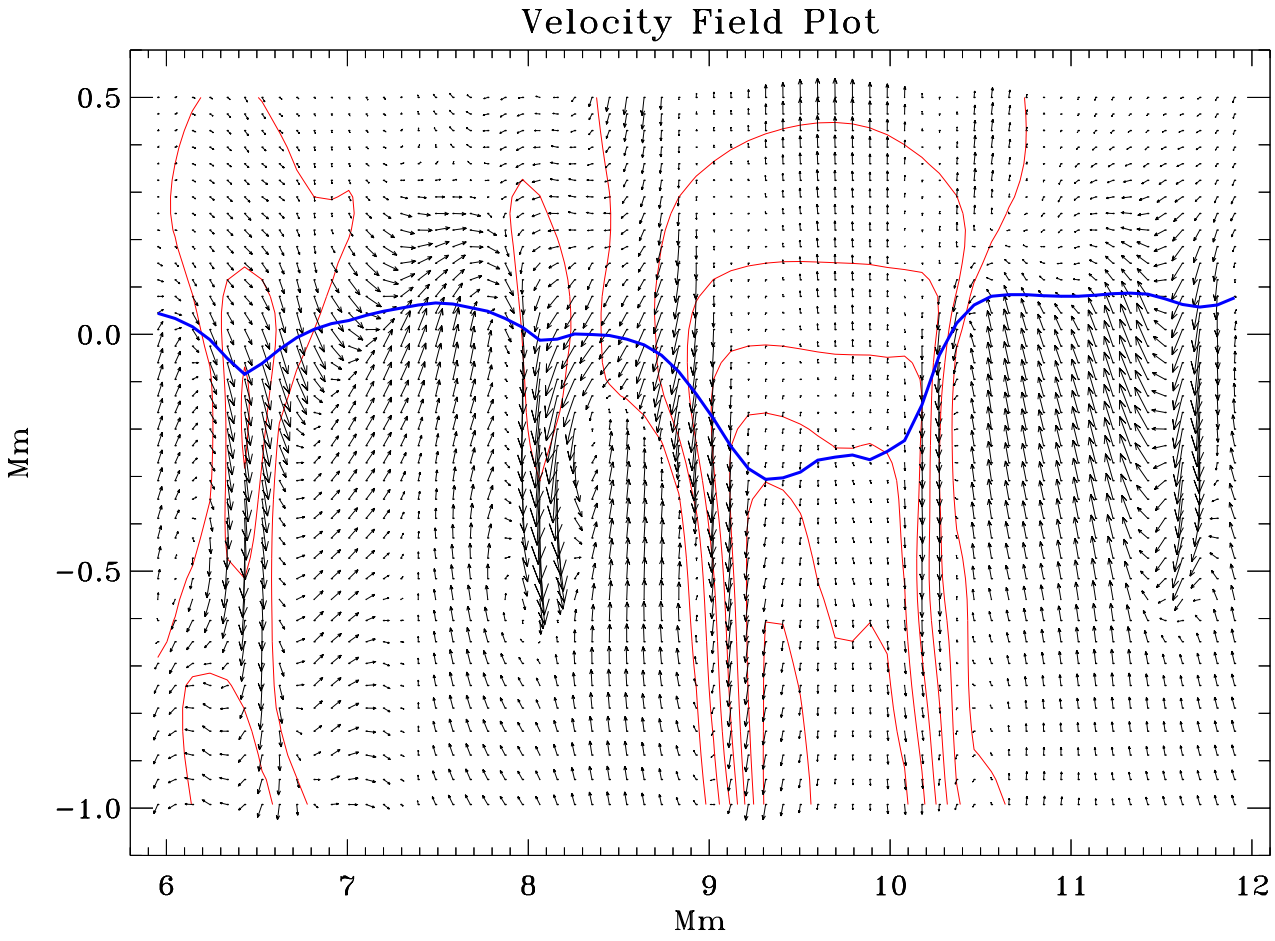

Figure 31: Velocity vectors and magnetic field contours (red) in bright point (left) and micropore (right). The flow is suppressed in the micropore, but not in the bright point.

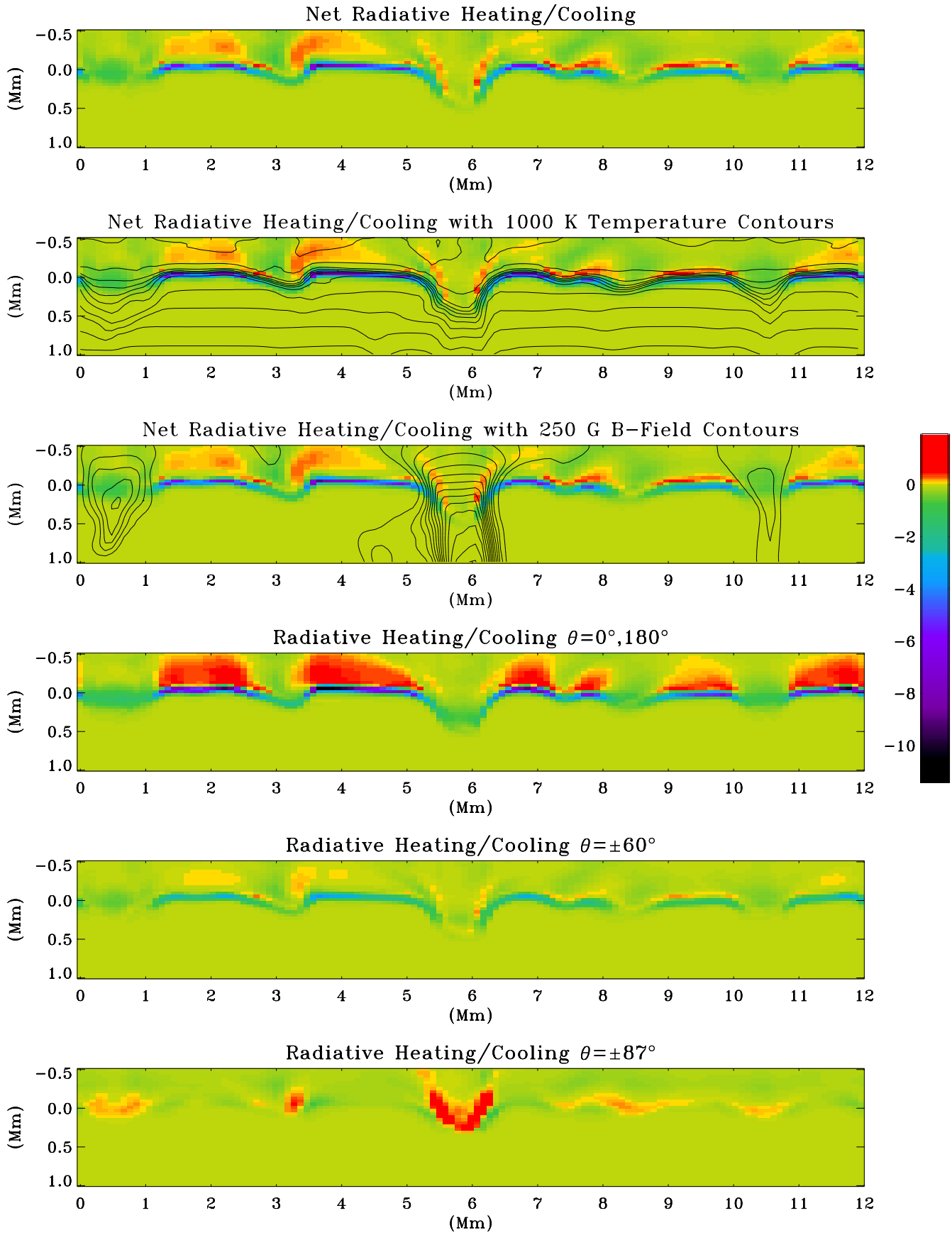

Figure 32: Radiative heating (red) and cooling (blue & purple). Micropore cools vertically and are heated from the sides.

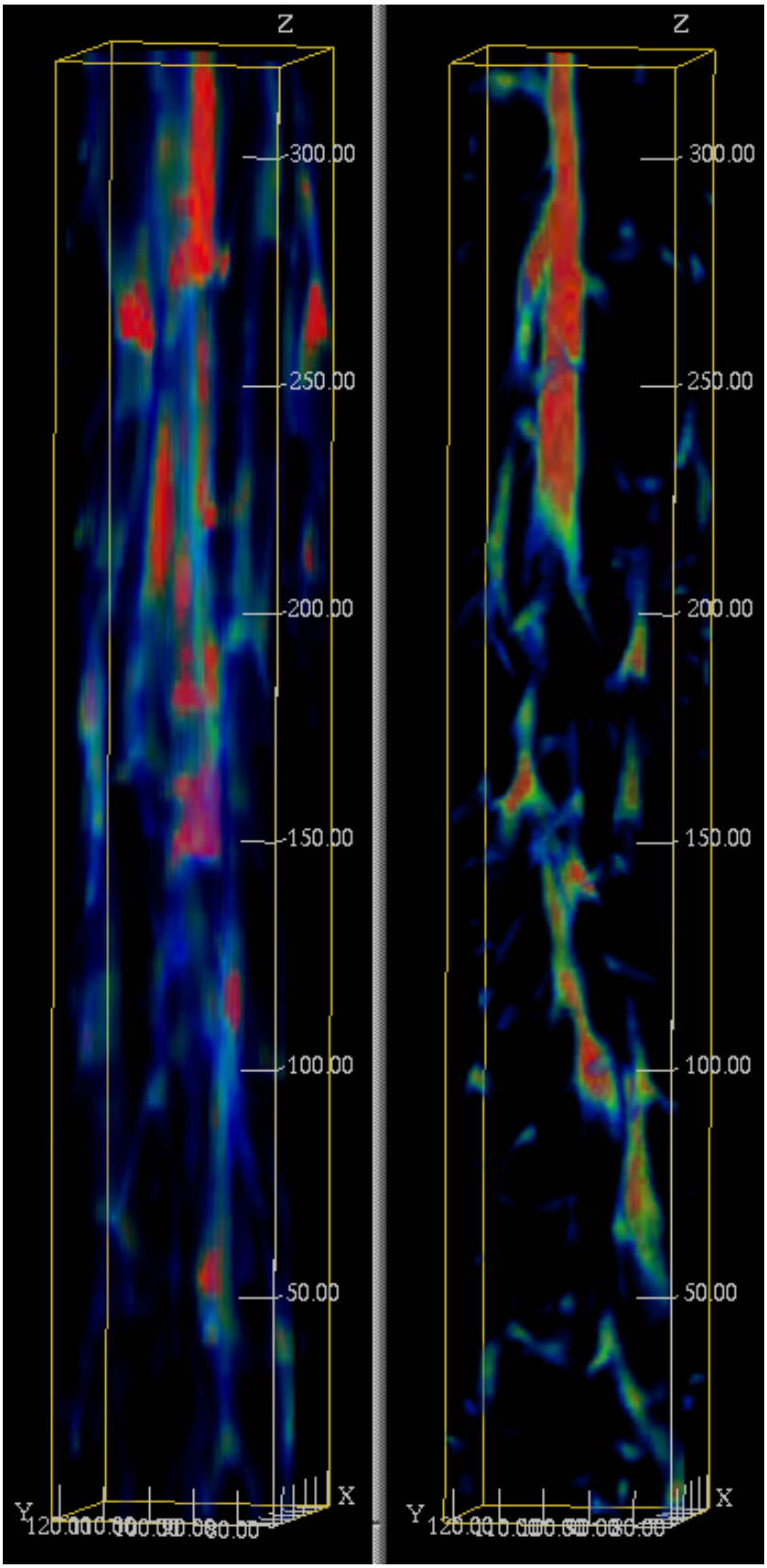

Figure 33: Evolution of surface magnetic field (left) and emergent intensity (right). Red is strong field and low (dark) intensity. Area is approximately 2x2 Mm. Vertical scale is time in units of 1/2 minute.

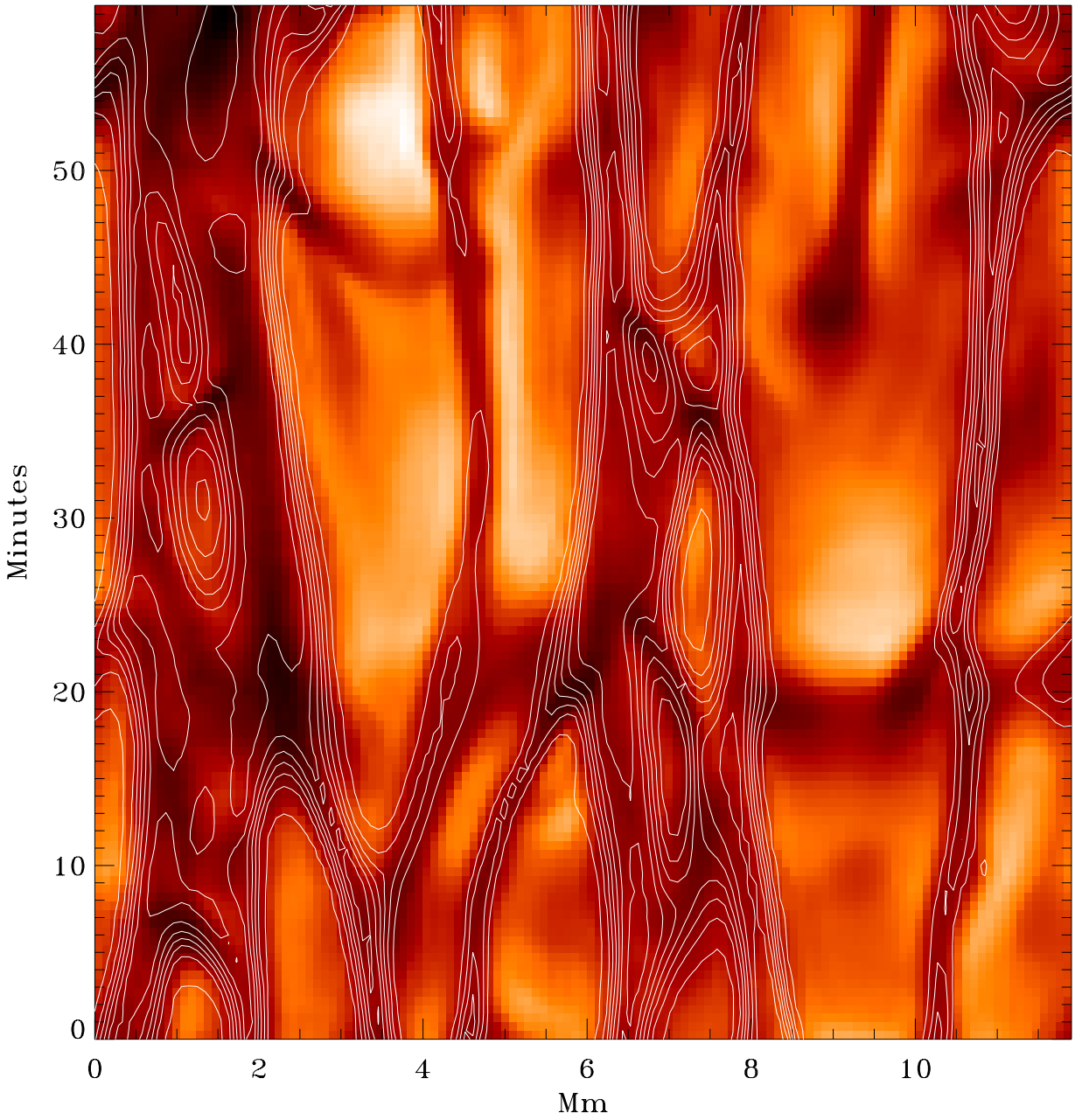

Figure 34: Evolution of the magnetic field and intensity in a slice through the micropore.

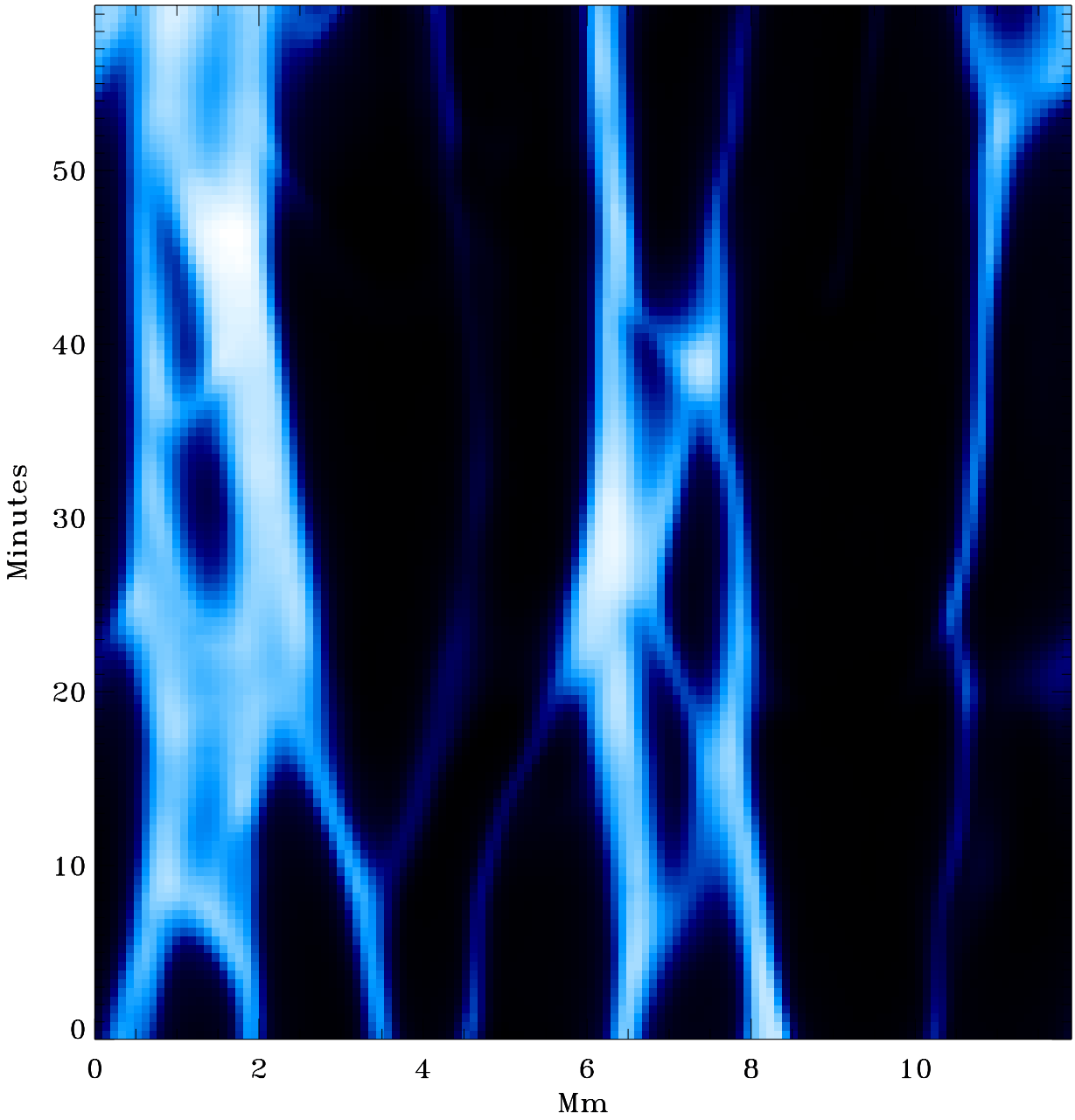

Figure 35: Evolution of just the magnetic field in a slice through the micropore.

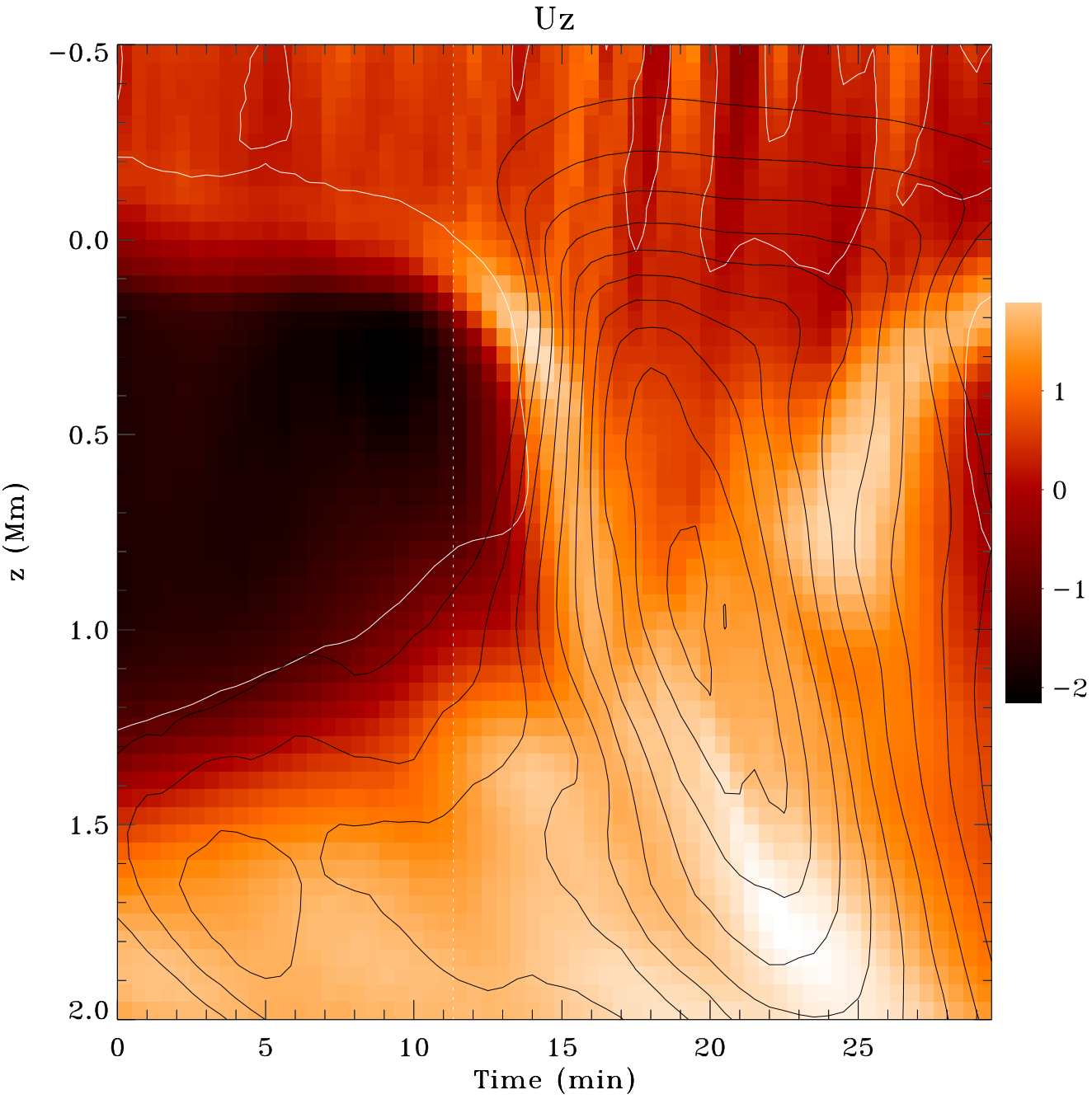

Figure 36: Evolution of the vertical velocity on a line through the center of the micropore. Contours are magnetic field strength.

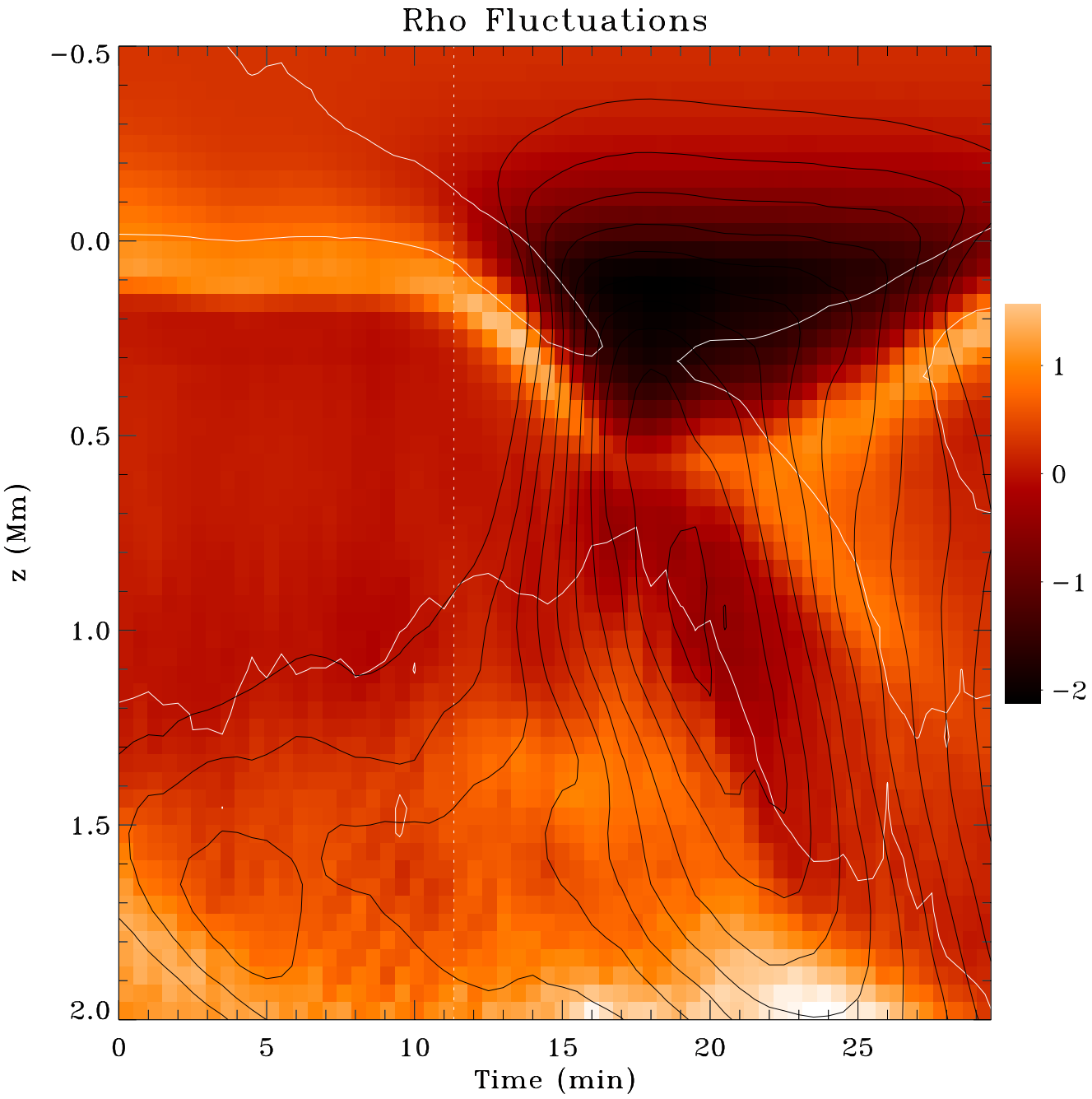

Figure 37: Evolution of the density fluctuations on a line through the center of the micropore.

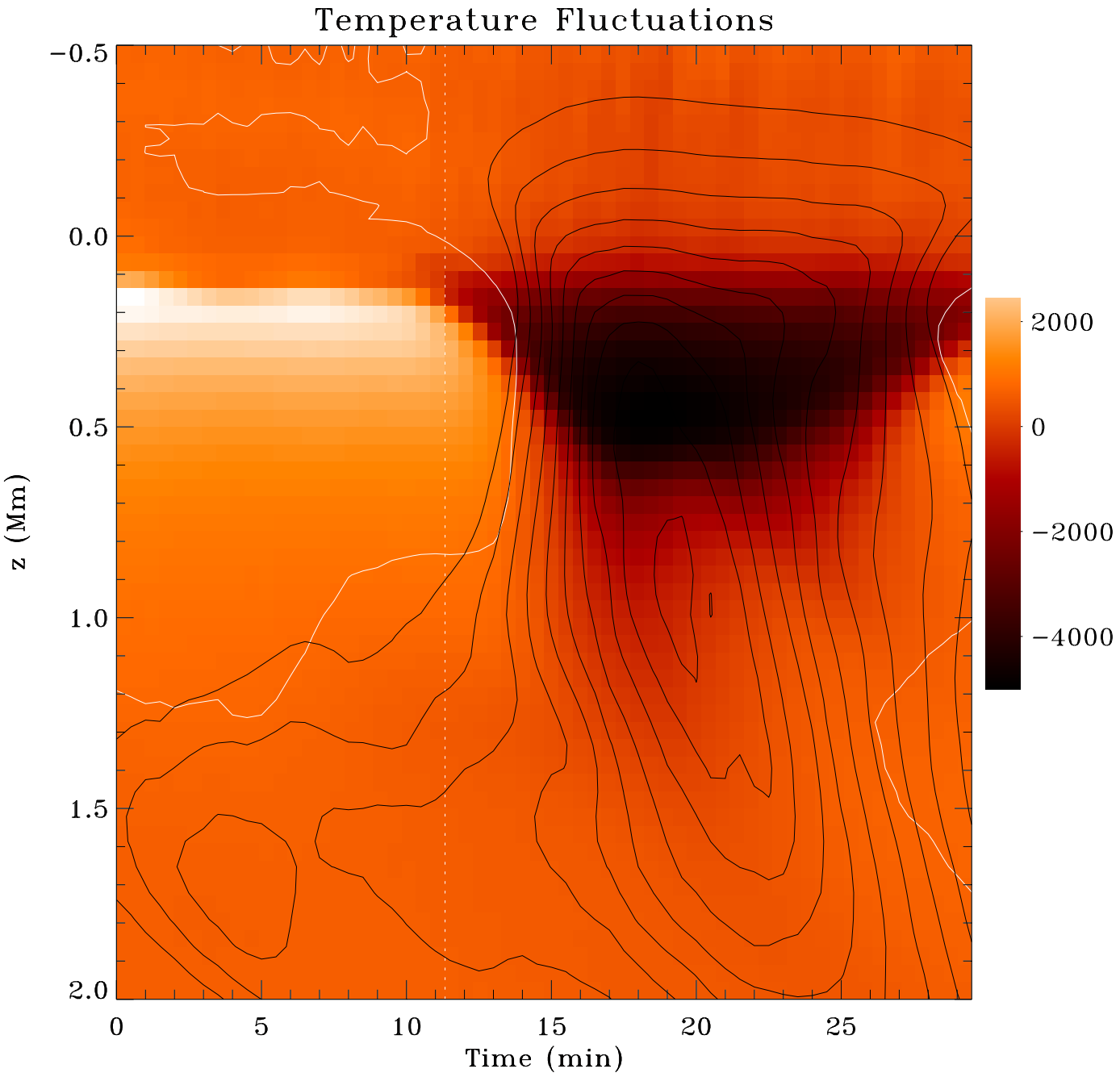

Figure 38: Evolution of the temperature fluctuations on a line through the center of the micropore.

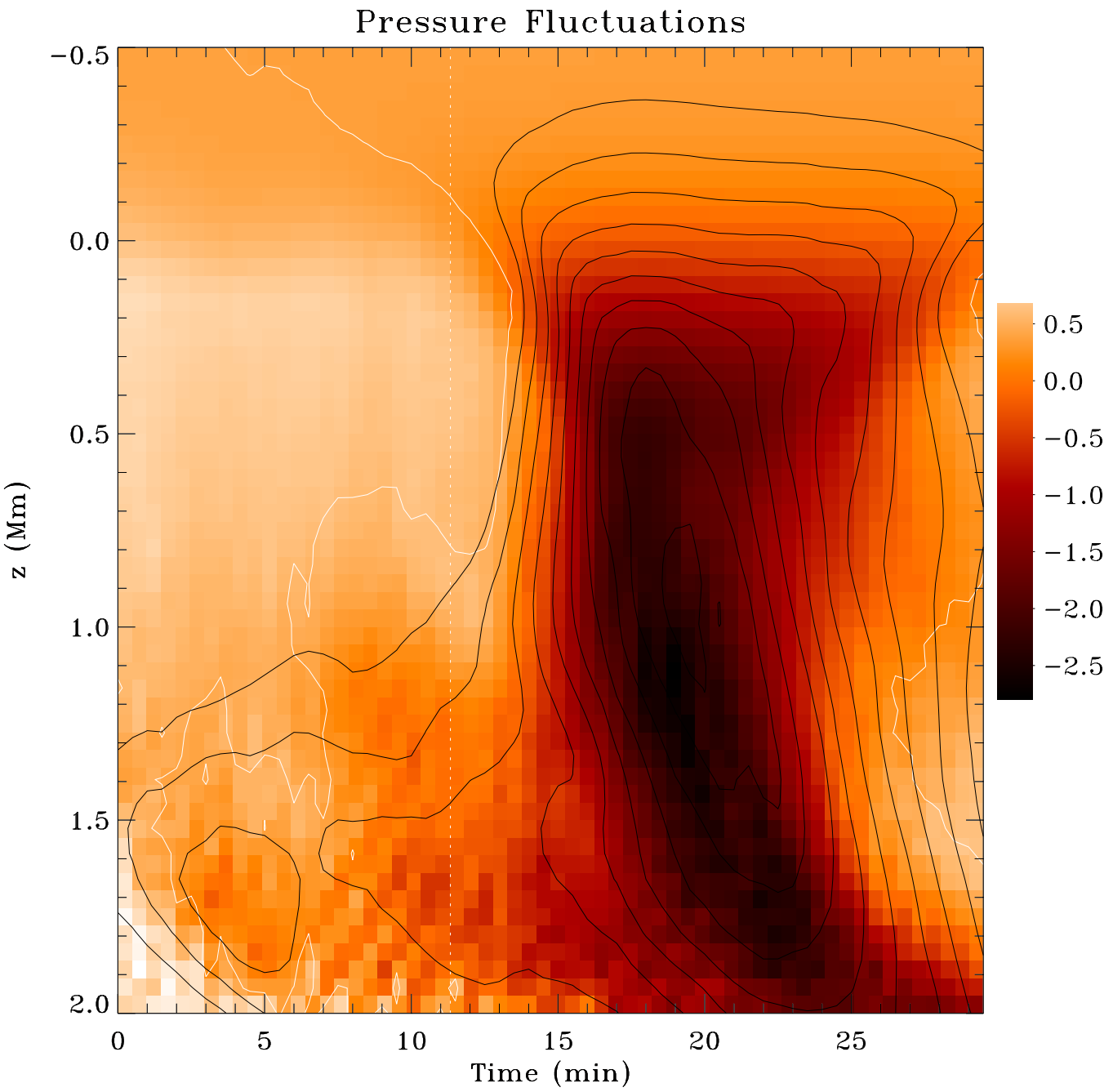

Figure 39: Evolution of the pressure fluctuations on a line through the center of the micropore.

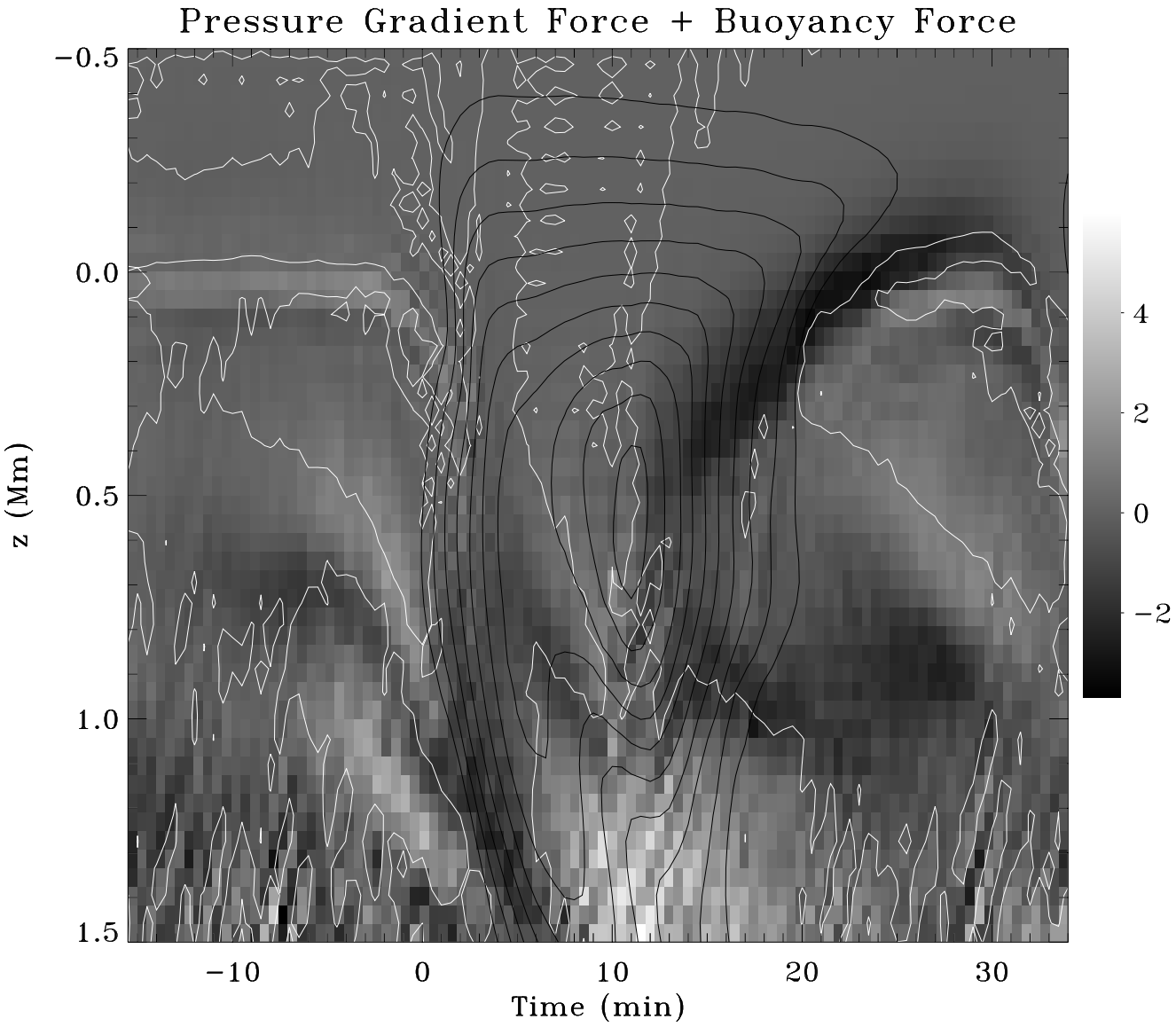

Figure 40: Pressure gradient plus buoyancy force as a function of depth and time at the center of the micropore. The fluctuation in the buoyancy force is downward both during the formation and dissolution of the micropore. The fluctuation in the pressure gradient force is upward during both the formation and dissolution of the micropore. The net pressure plus buoyancy force is slightly downward at the surface and strongly upward deep below the surface during the formation of the micropore. It is strongly upward during the dissolution of the micropore.

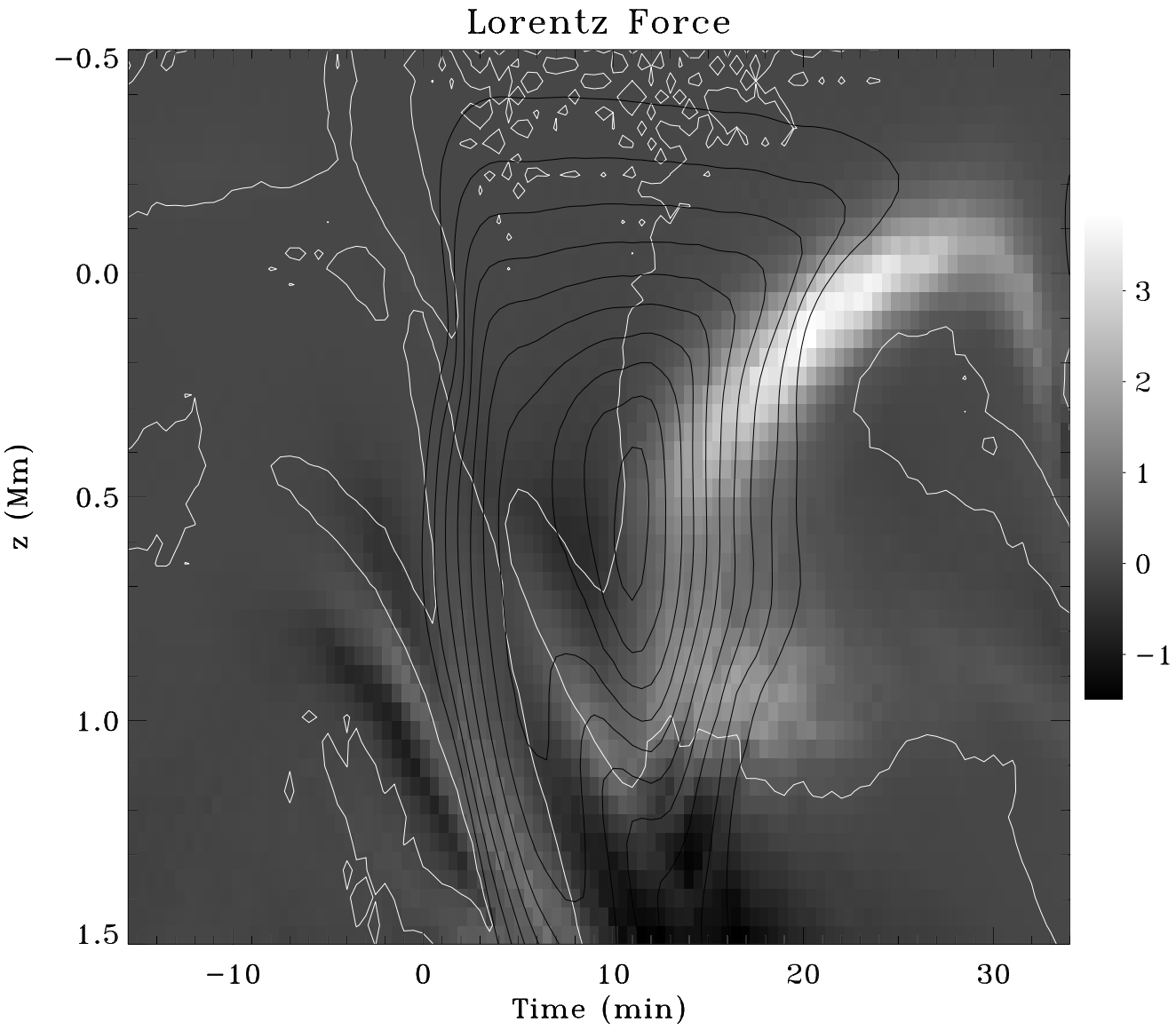

Figure 41: Lorentz force as a function of depth and time at the center of the micropore. The Lorentz force is small during the formation of the micropore. It is strongly downward during the dissolution of the micropore.

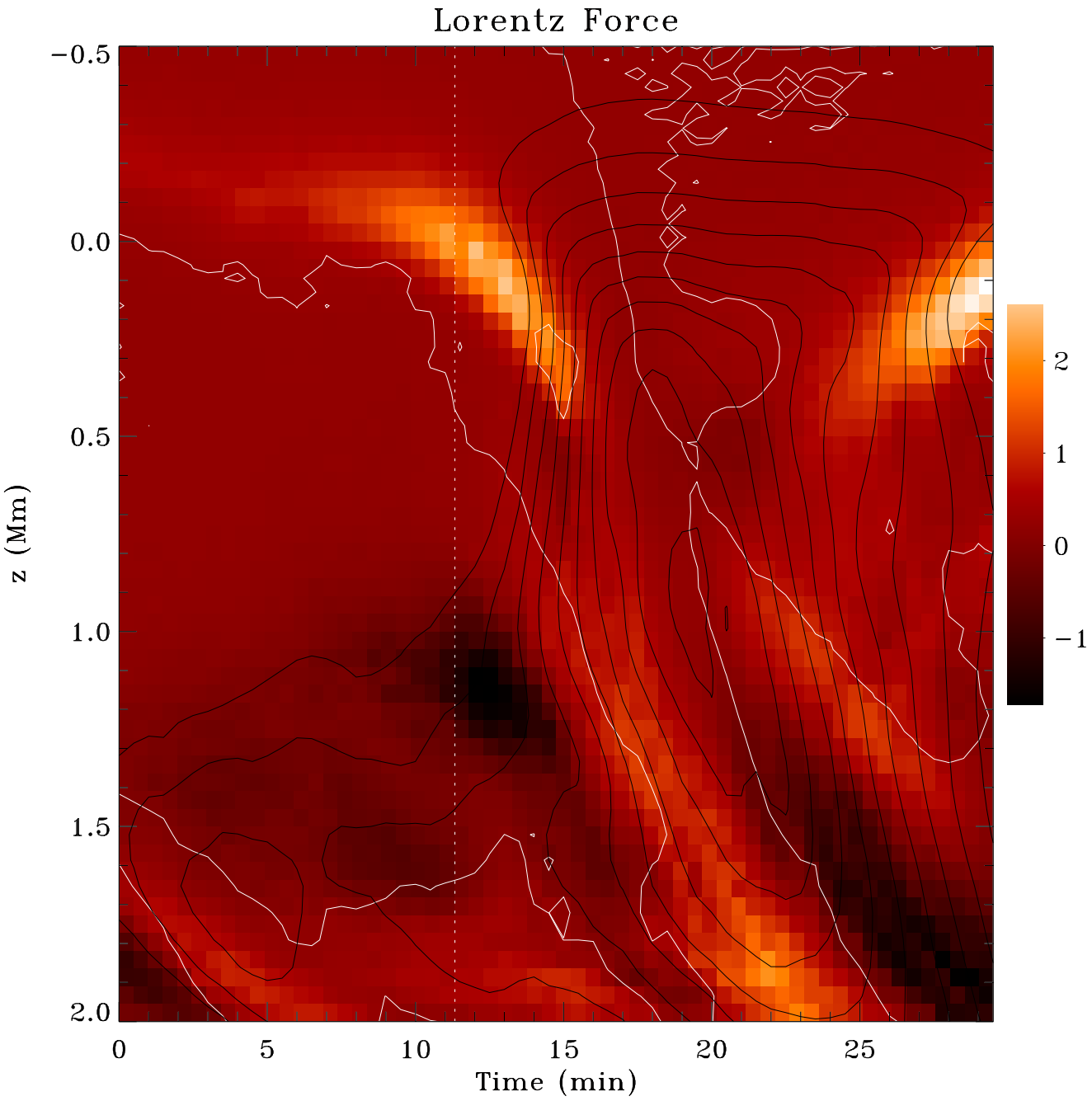

Figure 42: Lorentz force.

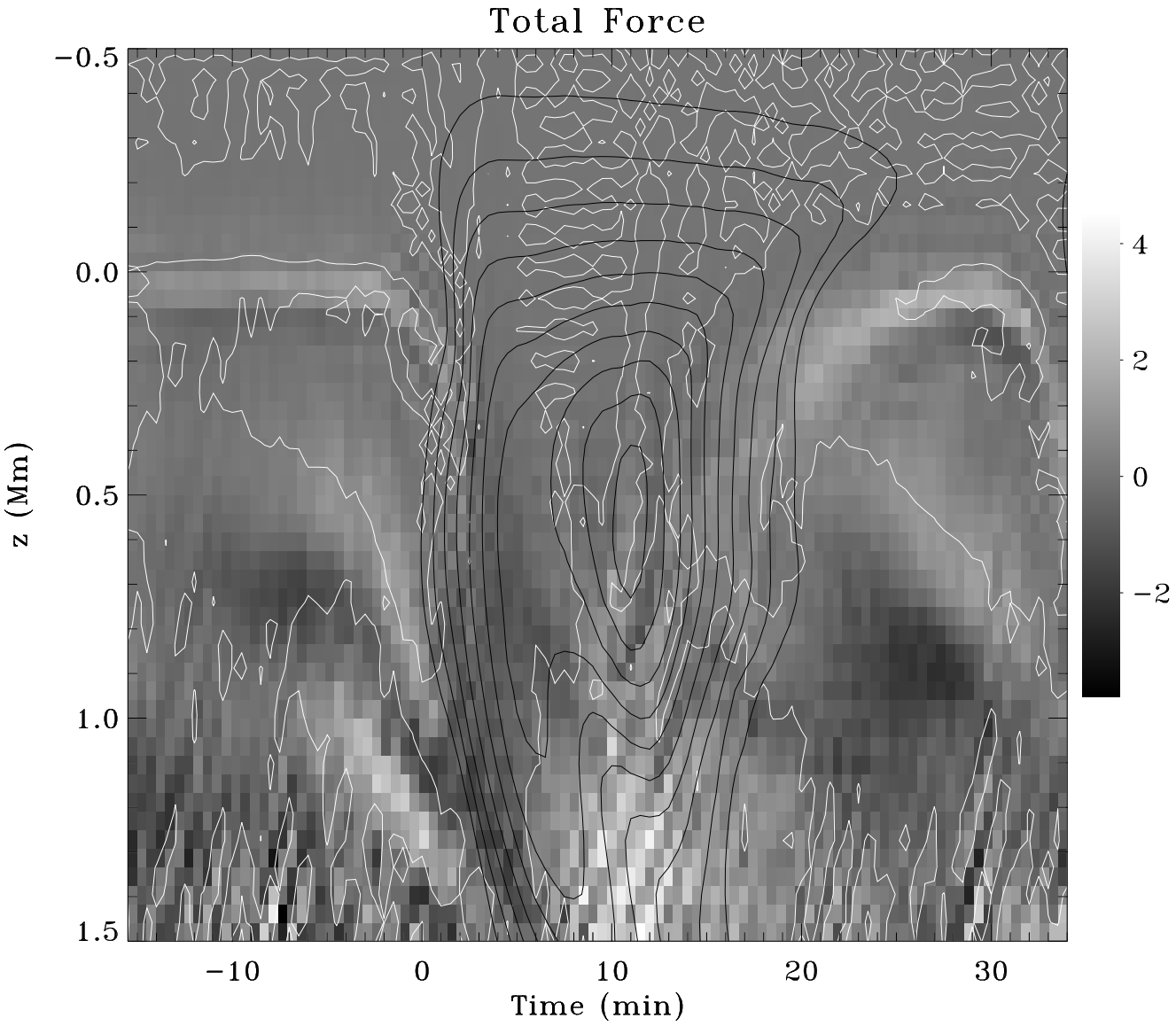

Figure 43: Total force – pressure + buoyancy + Lorentz – as a function of depth and time at the center of the micropore. The net total force is downward near the surface both during the formation and dissolution of the micropore and it is upward deep below the surface during the formation of the micropore.

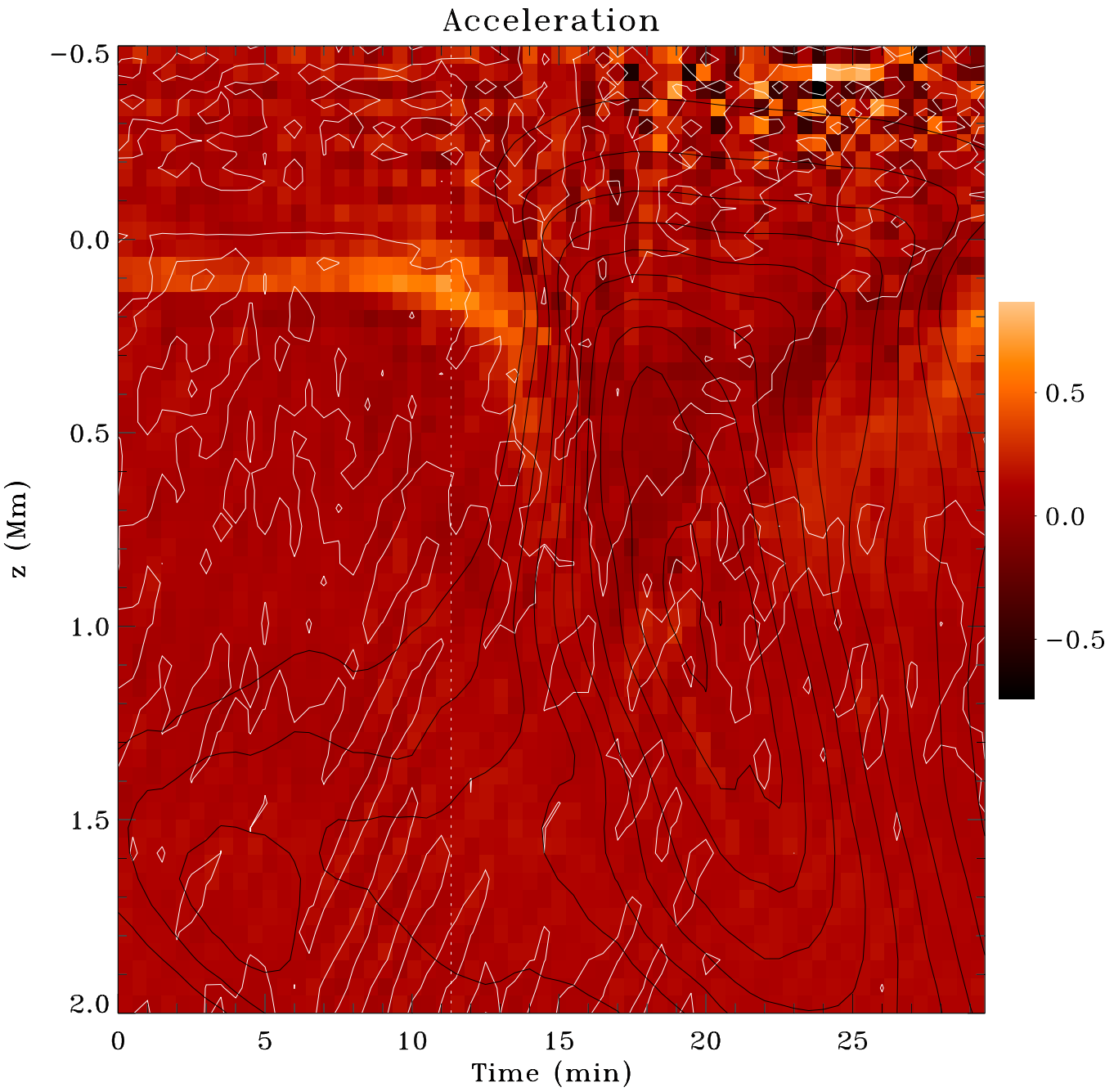

Figure 44: Acceleration.